



Removal of Singularities in Hoek-Brown Criterion and Its Numerical Implementation and Applications

Zi-Hang Dai¹; Tao You²; Xiang Xu³; and Qiao-Chuan Zhu⁴

Abstract: The representation of the Hoek-Brown criterion is an irregular curved hexagonal pyramid in the principal stress space, which leads to the occurrence of numerical singularities on the edges of the pyramid. With the aim of achieving a physical approximation to the pyramid, this study used both the C1 and C2 smoothing artifices on its sharp edges, and it was found that they were able to successfully eliminate the singularity and ensure the convexity of the yield surface. Meanwhile, to reflect the characteristic of the poor tensile strength of a rock mass, a tension cutoff surface was employed to form the whole modified combined yield surface. To facilitate comprehension and programming, the initial Hoek-Brown criterion and the smoothing and tension cutoff yield functions were all expressed in terms of stress invariants. The fully implicit backward Euler integral regression algorithm was employed to form the consistent stiffness matrix to ensure the high accuracy and fast convergence of numerical computations. In accordance with the failure zone in which a trial stress may fall, it may be pulled back to the initial Hoek-Brown yield surface, the transitional rounding yield surface, the tension cutoff yield surface, or the vertices that are the intersections of the former two with the latter. Furthermore, to facilitate the application of this modified Hoek-Brown criterion, a three-dimensional (3D) user-defined material behavior subroutine was developed in a finite-element program, and its reliability and applicability were verified through the numerical simulations of the triaxial compression and uniaxial tension tests of a rock and the excavation of a rock tunnel. **DOI:** [10.1061/\(ASCE\)GM.1943-5622.0001201](https://doi.org/10.1061/(ASCE)GM.1943-5622.0001201). © 2018 American Society of Civil Engineers.

Author keywords: Hoek-Brown criterion; Numerical singularity; Yield surface; Tension cutoff; Consistent stiffness matrix.

Introduction

The study of theories of rock strength originated in the eighteenth century, and the strength criterion of rock is an important part of these theories. Since then, a variety of theoretical and/or empirical strength criteria emerged successively. In many circumstances, theoretical strength criteria are unable to accurately describe the property of rock failure, and some parameters involved are difficult to determine in practical applications (Ramamurthy et al. 1988), so empirical criteria are valued by many researchers. It has been realized by geotechnical engineers that the failure envelopes of many geomaterials are curved, especially in the range of small normal stresses, and this has been experimentally demonstrated in the laboratory or field for many soft or stiff soils and for rocks or compacted rockfills (Anyagbunam 2015). Currently, the commonly used method, however, is to approximate experimental data with linear Mohr-Coulomb envelopes. The flaw is, however, evident because cohesions obtained by fitting with linear Mohr-Coulomb envelopes are usually overly large in

comparison with their actual values, and as a result, the strengths of geomaterials will be overestimated (Lefebvre 1981; Charles and Soares 1984). Baker's (2004) study shows that in the range of small principal stresses, only nonlinear envelopes can fit experimental results well. Therefore, many researchers have presented criteria for nonlinear failure. In 1980, based on the statistical analyses of a large number of laboratory triaxial tests of rocks and field tests of rock masses, E. Hoek and E. T. Brown presented the Hoek-Brown strength criterion (Hoek and Brown 1980), which currently is the criterion with the most significant influence and the broadest application. Later on, this criterion was improved by many researchers, including Hoek and Brown themselves, and applied in various engineering projects, such as slopes and tunnels. The main reasons for the wide use of this criterion are as follows: (1) it can synthetically consider the influences of many factors, such as the rock structure, rock strength, and stress state; (2) the material parameters can be obtained by simple field observations and laboratory uniaxial compression tests; and (3) it can be adjusted to provide an estimate of the decreased strength of the rock mass and reflect the intrinsic nonlinear strength criterion of rock and rock-mass failure characteristics. In addition, this criterion is applicable to the low-stress zone and the tensile-stress zone (Hoek et al. 2002; Thorsen 2013; Zou and Yu 2016). Over the past decades, this criterion was, however, applied mainly in analytical calculations of some relatively simple problems involving rock mechanics. With the fast development of numerical computation software, the constitutive model of rock based on the Hoek-Brown criterion has already been embedded into some commercial programs, such as *FLAC* and *PLAXIS*. Apparently, such advancements have greatly promoted the application of this criterion in numerical analyses of complex rock engineering problems.

The Hoek-Brown criterion represents a hexagon with slightly curved sides on the π plane, somewhat like the Mohr-Coulomb criterion, and a curved hexagonal pyramid in the principal stress space, which is different from the hexagonal pyramid of the latter. As a

¹Professor, School of Civil Engineering, Fuzhou Univ., Fuzhou 350108, P. R. China (corresponding author). Email: dzhang@fzu.edu.cn

²Ph.D. Candidate, College of Civil and Transportation Engineering, Hohai Univ., Nanjing 210098, P. R. China, and Key Laboratory of Ministry of Education for Geomechanics and Embankment Engineering, Hohai Univ., Nanjing 210098, P. R. China. Email: 1009727098@qq.com

³Lecturer, College of Transportation and Civil Engineering, Fujian Agriculture and Forestry Univ., Fuzhou 350108, P. R. China. Email: xuxiang20040071@126.com

⁴Engineer, Xi'an Changqing Technology Engineering Co., Xi'an 710021, P. R. China. Email: 769480@qq.com

Note. This manuscript was submitted on March 2, 2017; approved on February 1, 2018; published online on July 25, 2018. Discussion period open until December 25, 2018; separate discussions must be submitted for individual papers. This paper is part of the *International Journal of Geomechanics*, © ASCE, ISSN 1532-3641.

result, the Hoek-Brown criterion is more complex than the Mohr-Coulomb criterion, and certainly, like the latter, numerical difficulties will be encountered as the Lode angle θ approaches $\pm 30^\circ$ (edges of curved hexagonal pyramid) because the plastic flow vector \mathbf{a} is not uniquely defined for these stress combinations, or in other words, some constants included in the expression of \mathbf{a} become indeterminate. So far, there have been three types of approaches to overcome this kind of numerical singularity: (1) some smooth and continuous surfaces are employed to approximate the yield or potential surfaces, for example, a regular circular cone (Drucker and Prager 1952; Alejano and Bobet 2012), or other smooth convex surfaces (Wan 1992; Nayak and Zienkiewicz 1972; Matsuoka and Nakai 1974; Lade and Duncan 1975; Menetrey and Willam 1995) are used to replace the hexagonal pyramid of the Mohr-Coulomb criterion; (2) an original singular surface is used except in the vicinity of its edges, where a circular cone or hyperbolic surface is employed (Owen and Hinton 1980; Abbo et al. 2011); (3) the original hexagon is regarded as separate planar surfaces, and the constitutive law is implemented as a multisurface function using the formulation of Koiter (1953) (see also Ristinmaa and Tryding 1993; Clausen et al. 2006). The former two approaches attempt to physically approximate the original surfaces, and in theory, the second one is more reasonable.

Because of the complexity brought by the nonlinear Hoek-Brown criterion, many researchers have presented some equivalent methods for the Hoek-Brown criterion, using the Mohr-Coulomb criterion (Hoek et al. 2002; Dawson et al. 2000; Fu and Liao 2010), and their results are usually compared with the results obtained by the Hoek-Brown criterion (Trivedi 2013; Yi et al. 2005). Comparisons, however, show that these equivalent methods always overrate the strength of geomaterials in both the low-stress zone and the high-stress zone (Benz et al. 2008). Therefore, without doubt, one should directly apply the Hoek-Brown criterion in analytical calculations and numerical analyses where possible. To facilitate the application of this criterion, this article presents two approaches for the removal of singularities based on the second perception mentioned previously. They are the C1 and C2 continuity smoothing methods, which can make the first- and/or second-order derivatives of the yield or potential functions with respect to the vector of stress be continuous, and their validity and the convexity of the proposed smooth surfaces are proven. Simultaneously, the tension cutoff is used to consider the feature of tension rather than shear failure as the stress acting on a rock fall in a region of relatively higher tensile stress. The C1 continuity modified combined criterion was numerically implemented in the finite-element program *Abaqus* by programming a user-defined material behavior subroutine (UMAT), and thus the verification and applications of the UMAT are provided as well.

Brief Introduction to Hoek-Brown Criterion

The Hoek-Brown criterion reflects the nonlinear relationship between the principal stresses under the ultimate failure state, which is initially expressed as (Hoek and Brown 1980)

$$\sigma_1 = \sigma_3 + \sigma_{ci} \left(\frac{m_i \sigma_3}{\sigma_{ci}} + 1 \right)^{0.5} \quad (1)$$

where $\sigma_1 \geq \sigma_2 \geq \sigma_3$; σ_{ci} = uniaxial compressive strength of the intact rock; and m_i = empirical parameter reflecting the degree of weakness of the rock mass, and its magnitude range has been suggested by Hoek and Brown, and the detailed method to obtain this value has also been provided (Hoek 1983, 1994).

To increase the applicability of this criterion in rock-mass engineering, some modifications have been made in regard to Eq. (1), and thus the so-called general Hoek-Brown criterion has been obtained as

$$\sigma_1 = \sigma_3 + \sigma_{ci} \left(m_b \frac{\sigma_1}{\sigma_{ci}} + s \right)^a \quad (2)$$

where s and a are parameters introduced to reflect the characteristics of the rock mass, and they may be determined by referring to the literature (Hoek et al. 2002).

In Eq. (2), compressive stress is considered to be positive, and usually, this stipulation is widely applied in rock mechanics and geological engineering. This article stipulates, however, the tensile stress to be positive in accordance with the convention of most finite-element programs, including *Abaqus*. Thus, the Hoek-Brown criterion can be rewritten as

$$F = \sigma_1 - \sigma_3 - \sigma_{ci} \left(s - m_b \frac{\sigma_1}{\sigma_{ci}} \right)^a = 0 \quad (3)$$

The uniaxial compressive strength can be obtained while letting $\sigma_1 = 0$:

$$\sigma_c = \sigma_{ci} s^a \quad (4)$$

The uniaxial tensile strength can be obtained while $\sigma_3 = 0$:

$$\sigma_{ut} = \frac{1}{2} \sigma_{ci} \left(-m_b + \sqrt{m_b^2 + 4s} \right), (a = 0.5) \quad (5)$$

And the biaxial or triaxial tensile strength can be obtained while letting $\sigma_1 = \sigma_2 = \sigma_3$:

$$\sigma_{bt} = \frac{s \sigma_{ci}}{m_b} \quad (6)$$

To facilitate the numerical implementation, Eq. (3) can be expressed in terms of stress invariants as

$$F = \frac{I_1}{3} m_b \sigma_{ci}^{1/a-1} + (2\sqrt{J_2} \cos \theta)^{1/a} + \sqrt{J_2} m_b \sigma_{ci}^{1/a-1} \left(\cos \theta - \frac{\sin \theta}{\sqrt{3}} \right) - s \sigma_{ci}^{1/a} = 0 \quad (7)$$

where I_1 = first stress invariant ($I_1/3 = p$, representing the magnitude of the hydrostatic stress); and J_2 = second deviatoric stress invariant.

Figs. 1(a–c) show the yield loci of the Hoek-Brown criterion in the principal stress space, deviatoric planes, and meridian plane, respectively. Fig. 1(c) represents a meridian plane passing through any two right opposite edges in Fig. 1(a), and $\tau_{\sigma t}$, $\tau_{\sigma c}$ represent the triaxial tensile strength and the triaxial compressive strength, respectively.

In Eq. (7), letting $a = 0.5$ yields

$$F = \frac{I_1}{3} m_b \sigma_{ci} + 4J_2 \cos^2 \theta + \sqrt{J_2} m_b \sigma_{ci} \left(\cos \theta - \frac{\sin \theta}{\sqrt{3}} \right) - s \sigma_{ci}^2 = 0 \quad (8)$$

In fact, Eq. (8) is the form of the initial Hoek-Brown criterion [Eq. (1)] in terms of stress invariants, and experience shows that the

initial Hoek-Brown criterion is fairly suitable for describing the yield or failure behavior of rock masses with a geological strength index (GSI) of greater than 25.0 (Hoek 1994).

Approach of C1 Continuous Smoothing

The present work is mainly aimed at the initial Hoek-Brown criterion, and thereby the following derivations are based on Eq. (8):

$$\tau_{\sigma} = \sqrt{2J_2} = \frac{\sqrt{\frac{2}{3}[m_b\sigma_{ci}\cos(30^\circ + \theta)]^2 - 8\left(\frac{1}{3}m_b\sigma_{ci} - s\sigma_{ci}^2\right)\cos^2\theta - \frac{\sqrt{6}}{3}m_b\sigma_{ci}\cos(30^\circ + \theta)}}{4\cos^2\theta} \quad (9)$$

Eq. (9) reflects the relationship between $\sqrt{2J_2}$ and θ . Actually, $\sqrt{2J_2}$ represents the distance from a point on the yield locus to the origin point in the deviatoric plane, as shown in Fig. 1(b), and therefore, by means of Eq. (9), it is easy to plot and formulate the yield focus in terms of polar coordinates.

The removal of singularities on an edge of the curved hexagonal pyramid may be achieved by employing part of a curved circular cone that has a common tip with the pyramid and is tangent to both of the adjacent surfaces intersecting at an edge of the pyramid. The curved circular cone is hard to plot in the principal stress space and thus was not pursued in this study. This artifice is, however, illustrated in Fig. 2, where the hexagon represents the locus in any deviatoric plane in Fig. 1(b), for example, the one denoted by solid lines. A circular arc was here employed to round off each corner of the hexagon to make the transition from one side to another smooth and continuous. The Lode angle of transition was assumed as θ_t (positive).

Establishing a planar rectangular coordinate system as in Fig. 2 and considering the sixfold symmetry of the hexagon, the following

derivations can be done only in a part $0 \leq \theta \leq 60^\circ$, for example, in the part $\angle CO'D$. The coordinates (x, y) of a point on the Hoek-Brown yield surface can be expressed in terms of the polar coordinates $(\sqrt{2J_2}, \theta)$ as

$$\begin{aligned} x &= \sqrt{2J_2} \cos(60^\circ - \theta) \\ y &= \sqrt{2J_2} \sin(60^\circ - \theta) \end{aligned} \quad (10)$$

Then, the slope of the tangent to the Hoek-Brown yield surface passing through the point can be expressed as

$$\frac{dy}{dx} = \frac{dy/d\theta}{dx/d\theta} = \frac{\partial\sqrt{2J_2}/\partial\theta \cdot \sin(60^\circ - \theta) - \sqrt{2J_2} \cdot \cos(60^\circ - \theta)}{\partial\sqrt{2J_2}/\partial\theta \cdot \cos(60^\circ - \theta) + \sqrt{2J_2} \cdot \sin(60^\circ - \theta)} \quad (11)$$

where $\partial\sqrt{2J_2}/\partial\theta$ can be obtained by the first-order partial derivative of Eq. (9), namely

$$\frac{\partial\sqrt{2J_2}}{\partial\theta} = \frac{-\frac{1}{3}(m_b\sigma_{ci})^2[1 - 2\cos(\theta + 30^\circ)\sin\theta] - 8(\sigma_m m_b\sigma_{ci} - s\sigma_{ci}^2)\cos^2\theta \sin\theta}{4\cos^3\theta \sqrt{\frac{2}{3}[m_b\sigma_{ci}\cos(\theta + 30^\circ)]^2 - 8\cos^2\theta(\sigma_m m_b\sigma_{ci} - s\sigma_{ci}^2)}} + \frac{\sqrt{6}m_b\sigma_{ci}[1 - 2\cos(\theta + 30^\circ)\sin\theta]}{24\cos^3\theta} \quad (12)$$

Thus, the coordinates (x_c, y_c) of the transition point T_c of the circular arc rounding off the outer apex D (see Fig. 2) and the slope K_c of the tangent to the circular arc passing through T_c can be, respectively, calculated as

$$\begin{aligned} x_c &= O'T_c \cos(60^\circ - \theta_t) \\ y_c &= O'T_c \sin(60^\circ - \theta_t) \end{aligned} \quad (13)$$

$$\begin{aligned} K_c &= \frac{dy_c}{dx_c} / \frac{dx_c}{d\theta_t} \\ &= \frac{\partial O'T_c / \partial \theta_t \cdot \sin(60^\circ - \theta_t) - O'T_c \cdot \cos(60^\circ - \theta_t)}{\partial O'T_c / \partial \theta_t \cdot \cos(60^\circ - \theta_t) + O'T_c \cdot \sin(60^\circ - \theta_t)} \end{aligned} \quad (14)$$

Setting $\theta = \theta_t$ in Eqs. (9) and (12) yields

$$O'T_c = \sqrt{2J_2} = \frac{\sqrt{\frac{2}{3}[m_b\sigma_{ci}\cos(30^\circ + \theta_t)]^2 - 8\left(\frac{1}{3}m_b\sigma_{ci} - s\sigma_{ci}^2\right)\cos^2\theta_t - \frac{\sqrt{6}}{3}m_b\sigma_{ci}\cos(30^\circ + \theta_t)}}{4\cos^2\theta_t} \quad (15)$$

$$\frac{\partial O'T_c}{\partial \theta_t} = \left\{ \begin{aligned} &-\frac{1}{3}(m_b\sigma_{ci})^2[1 - 2\cos(\theta_t + 30^\circ)\sin\theta_t] - 8(\sigma_m m_b\sigma_{ci} - s\sigma_{ci}^2)\cos^2\theta_t \sin\theta_t \\ &4\cos^3\theta_t \sqrt{\frac{2}{3}[m_b\sigma_{ci}\cos(\theta_t + 30^\circ)]^2 - 8\cos^2\theta_t(\sigma_m m_b\sigma_{ci} - s\sigma_{ci}^2)} \\ &+ \frac{\sqrt{6}m_b\sigma_{ci}[1 - 2\cos(\theta_t + 30^\circ)\sin\theta_t]}{24\cos^3\theta_t} \end{aligned} \right\} \quad (16)$$

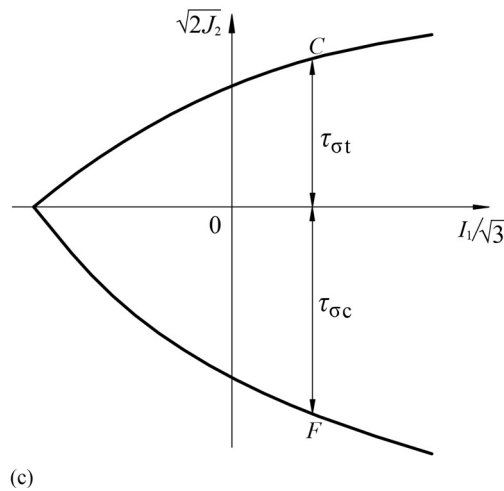
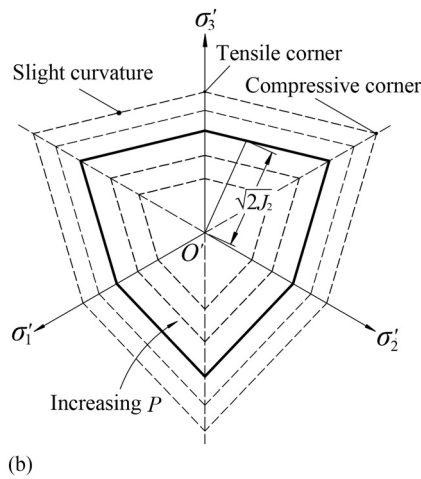
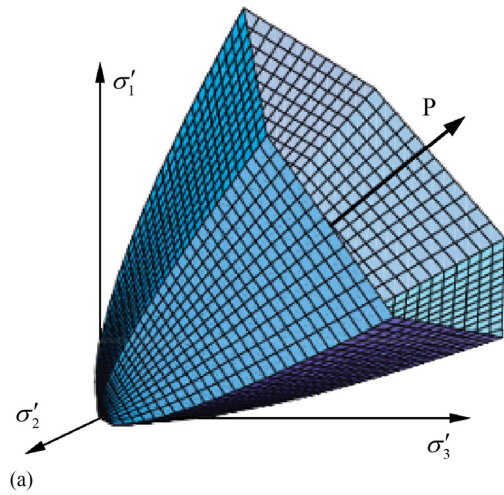


Fig. 1. Hoek-Brown yield loci: (a) principal stress space; (b) deviatoric planes; and (c) meridian plane.

Line $T_c O_c$ is perpendicular to the tangent mentioned previously and intersects the σ'_1 -axis ($y = x \cdot \tan 30^\circ$) at Point O_c . The slope of $T_c O_c$ can be expressed as

$$K_c^n = -\frac{1}{K_c} \quad (17)$$

Point O_c is the center of this circular arc, and its coordinates (x_{oc}, y_{oc}) can be calculated as

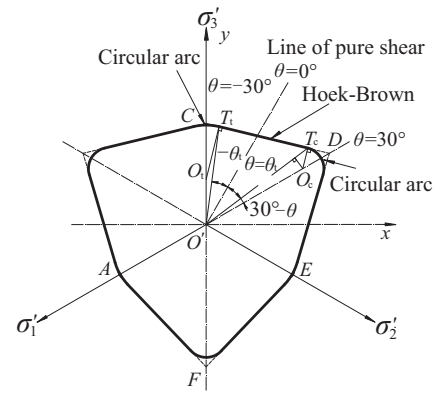


Fig. 2. Removal of singularities on corners.

$$\begin{aligned} x_{oc} &= \frac{\sqrt{3}(y_c - k_c^n x_c)}{1 - \sqrt{3}k_c^n} \\ y_{oc} &= \frac{y_c - k_c^n x_c}{1 - \sqrt{3}k_c^n} \end{aligned} \quad (18)$$

Virtually, in a deviatoric plane, the distance from the origin O' (see Fig. 2) to some point represents the vector radius of this point, and thus, from Fig. 2, one can get

$$O' O_c = \sqrt{x_{oc}^2 + y_{oc}^2} \quad (19)$$

The radius of the transitional circular arc can be expressed as

$$r_c = O_c T_c = \sqrt{(x_{oc} - x_c)^2 + (y_{oc} - y_c)^2} \quad (20)$$

Herein, one can obtain the yield function representing the transitional circular arc that can round off the apex D :

$$\begin{aligned} F_c &= \sqrt{2J_2} - \left\{ O' O_c \cos(30^\circ - \theta) \right. \\ &\quad \left. + \sqrt{r_c^2 - [O' O_c \sin(30^\circ - \theta)]^2} \right\} = 0 \end{aligned} \quad (21)$$

Substituting Eqs. (19) and (20) into Eq. (21) yields

$$\begin{aligned} F_c &= \sqrt{2J_2} - \left[\sqrt{x_{oc}^2 + y_{oc}^2} \cos(30^\circ - \theta) \right. \\ &\quad \left. + \sqrt{(x_{oc} - x_c)^2 + (y_{oc} - y_c)^2 - (x_{oc}^2 + y_{oc}^2) \sin^2(30^\circ - \theta)} \right] = 0 \end{aligned} \quad (22)$$

where (x_{oc}, y_{oc}) and (x_c, y_c) are, respectively, given by Eqs. (18) and (13); note that their values are variable with the magnitude of I_1 .

For cases where $-30^\circ \leq \theta \leq -\theta_t$, likewise, one can obtain analogous expressions.

The coordinates (x_t, y_t) of the transition point T_t of the circular arc rounding off the inner apex C (see Fig. 2), the slope K_t of the tangent to the circular arc passing through T_t , and the slope K_t^n of line $T_t O_t$ can be, respectively, calculated utilizing Eqs. (10), (11), and (17). The coordinates (x_{ot}, y_{ot}) of the center O_t of this circular arc can be expressed as

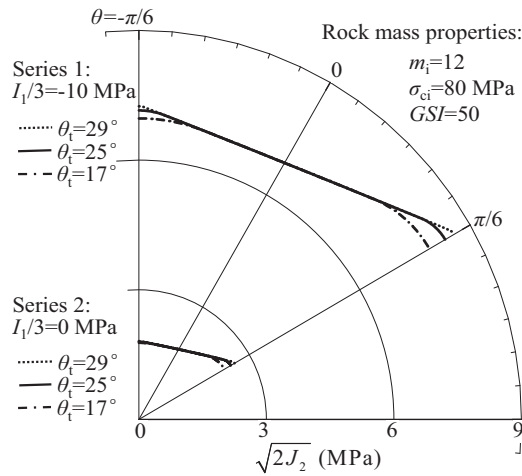


Fig. 3. C1 continuous rounding yield surfaces.

$$\begin{aligned} x_{ot} &= 0 \\ y_{ot} &= y_t - k_t^n x_t \end{aligned} \quad (23)$$

One can readily get

$$F = \begin{cases} \sqrt{2J_2} - \frac{\sqrt{\frac{2}{3}[m_b \sigma_{ci} \cos(30^\circ + \theta)]^2 - 8\left(\frac{I_1}{3}m_b \sigma_{ci} - s \sigma_{ci}^2\right) \cos^2 \theta - \frac{\sqrt{6}}{3}m_b \sigma_{ci} \cos(30^\circ + \theta)}}{4 \cos^2 \theta} = 0 & \text{for } -\theta_t \leq \theta \leq \theta_t \\ \sqrt{2J_2} - \left\{ O' O_c \cos(30^\circ - \theta) + \sqrt{r_c^2 - [O' O_c \sin(30^\circ - \theta)]^2} \right\} = 0 & \text{for } \theta_t < \theta \leq 30^\circ \\ \sqrt{2J_2} - \left\{ O' O_t \cos(30^\circ + \theta) + \sqrt{r_t^2 - [O' O_t \sin(30^\circ + \theta)]^2} \right\} = 0 & \text{for } -30^\circ \leq \theta < -\theta_t \end{cases} \quad (27)$$

Without a doubt, the first derivative of the previous yield function is continuous at the transition points T_c and T_t (i.e., C1 continuous). Fig. 3 demonstrates the C1 continuous smoothing in deviatoric planes employing the various transition angles ($\theta_t = 17, 25$, and 29° , respectively) at the two different hydrostatic stress levels (i.e., $I_1/3 = 0$ and 10 MPa). Obviously, the magnitude of transition angle θ_t controls the approaching extent of a circular arc to some corner, and when it is equal to or greater than 29° , the C1 continuous smoothing approximation is of sufficient precision, and it has been proven (see Appendix I) that a numerical singularity no longer exists.

According to indispensable conditions for Drucker's stability postulate, the rounded Hoek-Brown yield function must be convex. Similar to Abbo et al. (2011), the validation of convexity in Appendix II confirms that the proposed smoothing yield function meets the convex condition.

In this study, the potential function Q was assumed to have the same form as the yield function F , and the only difference was that parameters m_b and s in Eq. (27) (note that these two parameters are included in the expressions of $O'T_c$ and $O'T_t$ as well) were replaced with m_Q and s_Q , respectively. Prominently, when $m_Q = m_b$ and $s_Q = s$, then $Q = F$; that is, the associated flow rule is employed; otherwise, the nonassociated flow rule is used.

$$O' O_t = y_{ot} \quad (24)$$

$$r_t = O_t T_t = \sqrt{x_t^2 + (y_{ot} - y_t)^2} \quad (25)$$

Thus, likewise, one can easily obtain the following yield function representing the transitional circular arc that can round off the apex C:

$$\begin{aligned} F_t &= \sqrt{2J_2} - \left\{ O' O_t \cos(30^\circ + \theta) \right. \\ &\quad \left. + \sqrt{r_t^2 - [O' O_t \sin(30^\circ + \theta)]^2} \right\} \\ &= \sqrt{2J_2} - \left[y_{ot} \cos(30^\circ + \theta) \right. \\ &\quad \left. + \sqrt{x_t^2 + (y_{ot} - y_t)^2 - y_{ot}^2 \sin^2(30^\circ + \theta)} \right] = 0 \end{aligned} \quad (26)$$

where y_{ot} and (x_t, y_t) are also variable with the magnitude of I_1 and can be given by Eq. (23) and an equation similar to Eq. (13), respectively.

Therefore, the whole yield function after removing singularities can be outlined as follows:

Approach of C2 Continuous Smoothing

To formulate an elastoplastic constitutive matrix that is consistent with a global Newton-Raphson scheme, the yield and potential functions must meet the requirement of C2 continuity (Simo and Taylor 1985). For a smoothing function, of course, guaranteeing the C2 continuity at the transition points is the key to this problem. In view of the previous derivation of the C1 continuous approximation, a function that provides the C2 continuous smoothing approximation to the vertices in deviatoric planes can be constructed by adding some extra terms.

Rewrite Eq. (27) in the following form:

$$F = \begin{cases} \sqrt{2J_2} - f_0(I_1/3, \theta) = 0 & \text{for } -\theta_t \leq \theta \leq \theta_t \\ \sqrt{2J_2} - f_1(I_1/3, \theta, \theta_t) = 0 & \text{for } \theta_t < \theta \leq 30^\circ \\ \sqrt{2J_2} - f_2(I_1/3, \theta, -\theta_t) = 0 & \text{for } -30^\circ \leq \theta < -\theta_t \end{cases} \quad (28)$$

where f_0, f_1, f_2 denote the second term on the right side of each piecewise function in Eq. (27).

First, for the range of $\theta_t < \theta \leq 30^\circ$, a yield function was constructed as the second piecewise function in Eq. (29):

$$F = \begin{cases} \sqrt{2J_2} - f_0(I_1/3, \theta) = 0 & \text{for } -\theta_t \leq \theta \leq \theta_t \\ \sqrt{2J_2} - [a_1 + b_1 f_1(I_1/3, \theta, \theta_t) + c_1 \sin^2 3\theta] = 0 & \text{for } \theta_t < \theta \leq 30^\circ \end{cases} \quad (29)$$

where, in comparison with the second piecewise function in Eq. (28), two extra terms and three undetermined constant parameters a_1, b_1, c_1 were introduced, which can be determined by meeting the following conditions:

$$\begin{aligned} f_0 &= a_1 + b_1 f_1 + c_1 \sin^2 3\theta & \text{for } \theta = \theta_t \\ \frac{\partial f_0}{\partial \theta} &= b_1 \frac{\partial f_1}{\partial \theta} + 3c_1 \sin 6\theta & \text{for } \theta = \theta_t \\ b_1 \frac{\partial f_1}{\partial \theta} + 3c_1 \sin 6\theta &= 0 & \text{for } \theta = 30^\circ \\ \frac{\partial^2 f_0}{\partial \theta^2} &= b_1 \frac{\partial^2 f_1}{\partial \theta^2} + 18c_1 \cos 6\theta & \text{for } \theta = \theta_t \end{aligned} \quad (30)$$

The first two conditions can ensure the C1 continuity of the entire yield surface. In view of the previous section, it can be seen that the third condition can be satisfied with arbitrary values of a_1, b_1 , and c_1 . The last constraint condition can guarantee the consistency of the second derivative of the two piecewise functions in Eq. (29) at the transition point. By the use of Eq. (30), accordingly, the explicit expression of a_1, b_1, c_1 can be derived as

$$\begin{aligned} a_1 &= \bar{f}_0 - b_1 \bar{f}_1 - c_1 \sin^2 3\theta_t \\ b_1 &= \frac{6\bar{f}_0' \cos 6\theta_t - \bar{f}_0'' \sin 6\theta_t}{6\bar{f}_1' \cos 6\theta_t - \bar{f}_1'' \sin 6\theta_t} \\ c_1 &= \frac{\bar{f}_0'' \cdot \bar{f}_1' - \bar{f}_1'' \cdot \bar{f}_0'}{18\bar{f}_1' \cos 6\theta_t - 3\bar{f}_1'' \sin 6\theta_t} \end{aligned} \quad (31)$$

where \bar{f}_0 and \bar{f}_1 , respectively, denote the values of f_0, f_1 at $\theta = \theta_t$, and one can have $\bar{f}_0' = \bar{f}_1'$ because of the continuity; \bar{f}_0'', \bar{f}_1' , and \bar{f}_0'', \bar{f}_1'' imply, respectively, the first and second derivatives of f_0, f_1 with respect to θ in the case of $\theta = \theta_t$, and one can have $\bar{f}_0'' = \bar{f}_1''$; and note that all of them can be determined as long as the properties of a rock mass are known.

Thus, the composite yield function expressed by Eq. (29) is of C2 continuity, in which both the first and second derivatives are continuous at the transition angle θ_t .

Likewise, for the case $-\theta_t < \theta \leq -30^\circ$, the following equations can be easily constructed or deduced:

$$\begin{aligned} F &= \sqrt{2J_2} - [a_2 + b_2 f_2(I_1/3, \theta, \theta_t) + c_2 \sin^2 3\theta] \\ &= 0 \quad \text{for } -30^\circ \leq \theta \leq -\theta_t \end{aligned} \quad (32)$$

$$\begin{aligned} a_2 &= \bar{f}_0 - a_2 \bar{f}_2 - b_2 \sin^2 3\theta_t \\ b_2 &= \frac{6\bar{f}_0' \cos 6\theta_t - \bar{f}_0'' \sin 6\theta_t}{6\bar{f}_2' \cos 6\theta_t - \bar{f}_2'' \sin 6\theta_t} \\ c_2 &= \frac{\bar{f}_0'' \cdot \bar{f}_2' - \bar{f}_2'' \cdot \bar{f}_0'}{18\bar{f}_2' \cos 6\theta_t - 3\bar{f}_2'' \sin 6\theta_t} \end{aligned} \quad (33)$$

Combining Eqs. (29) and (32), the whole C2 continuous smoothing yield surface can be expressed as

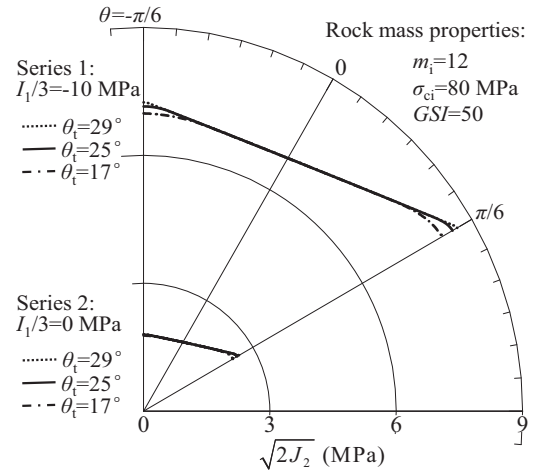


Fig. 4. C2 continuous smoothing yield surfaces.

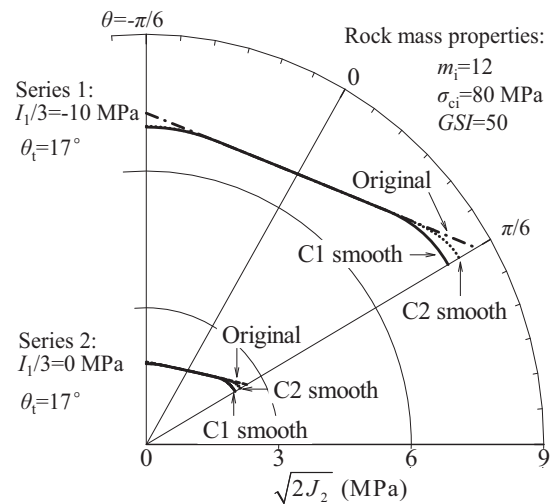


Fig. 5. Comparisons of yield loci between C1 and C2 continuous approximations.

$$F = \begin{cases} \sqrt{2J_2} - f_0(I_1/3, \theta) = 0 & \text{for } -\theta_t \leq \theta \leq \theta_t \\ \sqrt{2J_2} - [a_1 + b_1 f_1(I_1/3, \theta, \theta_t) + c_1 \sin^2 3\theta] = 0 & \text{for } \theta_t < \theta \leq 30^\circ \\ \sqrt{2J_2} - [a_2 + b_2 f_2(I_1/3, \theta, \theta_t) + c_2 \sin^2 3\theta] = 0 & \text{for } -30^\circ \leq \theta \leq -\theta_t \end{cases} \quad (34)$$

Note that the previous C1 continuous scheme is a special case that can be recovered by setting $b_1 = b_2 = 1$ and $a_1 = c_1 = a_2 = c_2 = 0$ in Eq. (34). Similar to Fig. 3, Fig. 4 shows the cases of the C2 smoothing. To gain a visible difference, a comparison between the C2 rounding and the C1 rounding when $\theta_t = 17^\circ$ is shown in Fig. 5. Obviously, in the vicinity of the apexes, the former can approach to the original yield surface more closely than the latter. Take Series 1, for example, for $\theta = 30^\circ$ (i.e., $\pi/6$), $\sqrt{2J_{2\text{orig}}}$, that is, the value of the $\sqrt{2J_2}$ of the outer apex on the original yield surface, is equal to 8.63 MPa, and correspondingly, $\sqrt{2J_{2\text{C2}}} = 8.18$ MPa and $\sqrt{2J_{2\text{C1}}} = 7.89$ MPa, so the maximum deviations for the C2 and C1 rounding approaches are 5.2 and 8.6%, respectively. Further comparison shows that the corresponding maximum deviations will be reduced to 0.358 and 0.811%, respectively, if assuming $\theta_t = 29^\circ$.

To facilitate a global Newton-Raphson scheme, the second-order derivative of the potential function ought to be determined in advance. As shown in Appendix II, it was found that this C2 continuous composite yield function will not cause the problem of numerical singularity because the subsistent indeterminate terms in the original yield function no longer occur. Meanwhile, it is worth noting that Eq. (29) describes an unconditional convex yield function, which is verified in Appendix II.

Constitutive Integral Algorithm

In numerical computation, with the increase of loading, the stresses of some Gauss points in a model may exceed yield stresses, simultaneously accompanied by plastic strains. The real stress of a point cannot, however, exceed a certain yield stress under the control of yield criterion, so the stress point can only move on the yield surface as yield takes place. Thereby, those points whose stresses exceed yield stresses must be adjusted to return to the yield surface, and the method of adjustment is the constitutive integral algorithm, also known as the stress-update algorithm (Belytschko et al. 2000). The explicit and implicit algorithms are the two commonly used algorithms. The implicit return-mapping scheme, which may avoid the phenomenon of stress drift that the explicit algorithm may lead to, was employed in this study to obtain accurate values; a quadratic convergence can be obtained in use of the Newton-Raphson iteration, and its accuracy and stability are higher as well. The fully implicit backward Euler integral regression algorithm may be written as

$$\begin{aligned}\boldsymbol{\varepsilon}_{n+1} &= \boldsymbol{\varepsilon}_n + \Delta\boldsymbol{\varepsilon} \\ \boldsymbol{\varepsilon}_{n+1}^p &= \boldsymbol{\varepsilon}_n^p + \Delta\lambda_{n+1}\mathbf{r}_{n+1} \\ a_{n+1} &= a_n + \Delta\lambda_{n+1}h_{n+1} \\ \boldsymbol{\sigma}_{n+1} &= \mathbf{D} : (\boldsymbol{\varepsilon}_{n+1} - \boldsymbol{\varepsilon}_{n+1}^p) \\ F_{n+1} &= F(\boldsymbol{\sigma}_{n+1}, a_{n+1}) = 0\end{aligned}\quad (35)$$

The formula in Eq. (35) denotes the solutions of $(\boldsymbol{\varepsilon}_{n+1}, \boldsymbol{\varepsilon}_{n+1}^p, a_{n+1})$ at the time step $n+1$, obtained by the nonlinear algebraic equations on the basis of the solutions of $(\boldsymbol{\varepsilon}_n, \boldsymbol{\varepsilon}_n^p, a_n)$ at the previous time step n and the incremental strain $\Delta\boldsymbol{\varepsilon}$ at this time step. The updated variables come from the convergent values at the previous time step. From the second equation in Eq. (35), one may have

$$\Delta\boldsymbol{\varepsilon}_{n+1}^p \equiv \boldsymbol{\varepsilon}_{n+1}^p - \boldsymbol{\varepsilon}_n^p = \Delta\lambda_{n+1}\mathbf{r}_{n+1} \quad (36)$$

Substituting Eq. (36) into Eq. (35) yields

$$\begin{aligned}\boldsymbol{\sigma}_{n+1} &= \mathbf{D} : (\boldsymbol{\varepsilon}_{n+1} - \boldsymbol{\varepsilon}_n^p - \Delta\boldsymbol{\varepsilon}_{n+1}^p) = \mathbf{D} : (\boldsymbol{\varepsilon}_n - \boldsymbol{\varepsilon}_n^p) + \mathbf{D} : \Delta\boldsymbol{\varepsilon} - \mathbf{D} : \Delta\boldsymbol{\varepsilon}_{n+1}^p \\ &= (\boldsymbol{\sigma}_n + \mathbf{D} : \Delta\boldsymbol{\varepsilon}) - \mathbf{D} : \Delta\boldsymbol{\varepsilon}_{n+1}^p \\ &= \boldsymbol{\sigma}_{n+1}^{\text{trial}} - \mathbf{D} : \Delta\boldsymbol{\varepsilon}_{n+1}^p \\ &= \boldsymbol{\sigma}_{n+1}^{\text{trial}} - \Delta\lambda_{n+1}\mathbf{D} : \mathbf{r}_{n+1}\end{aligned}\quad (37)$$

where $\boldsymbol{\sigma}_{n+1}^{\text{trial}}$ = trial elastic stress; and $-\Delta\lambda_{n+1}\mathbf{D} : \mathbf{r}_{n+1}$ = amount of plastic correction, which returns or projects on the updated yield surface along the flow direction of the plasticity of the endpoint, as shown in Fig. 6.

The basic formula using the backward Euler integral regression algorithm to pull a stress point (e.g., the point B) back to the yield surface is given by

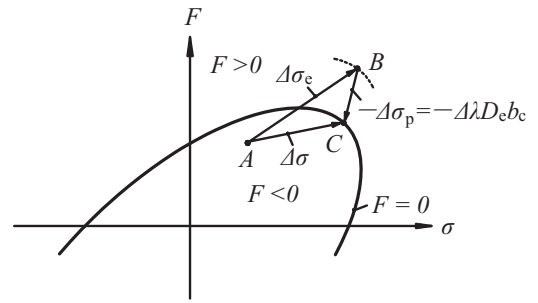


Fig. 6. Principle of return mapping.

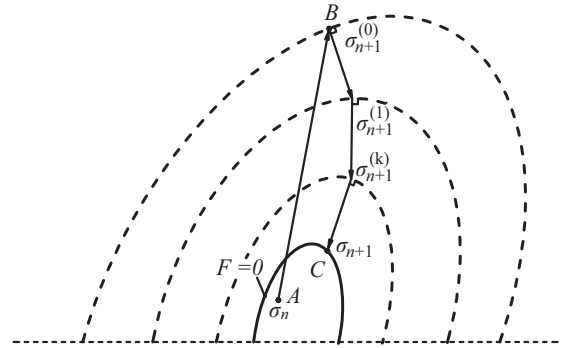


Fig. 7. Iteration scheme for plastic correction.

$$\boldsymbol{\sigma}_C = \boldsymbol{\sigma}_B - \Delta\lambda\mathbf{D}_e\mathbf{b}_C \quad (38)$$

As shown in Fig. 7, the predictor point $\boldsymbol{\sigma}_C$ can be given by the initial computation:

$$\boldsymbol{\sigma}_C = \boldsymbol{\sigma}_B - \Delta\lambda\mathbf{D}_e\mathbf{b}_B \quad (39)$$

where $\mathbf{b}_B = \partial Q / \partial \boldsymbol{\sigma}$, representing the first-order derivative of the potential function.

Usually, the initial estimated value of the stress $\boldsymbol{\sigma}_C$ will not lie on the yield surface, so it needs to return to the yield surface. The stress, elastic strain, and plastic strain will be updated one time after each iteration until the stress point falls in the range of a tolerant error; thus, it is deemed to have returned to the yield surface. The iteration scheme is illustrated in Fig. 7, the detailed iteration algorithm may be found in the literature (Clausen and Damkilde 2008; Borst et al. 2012), and the consistent tangential stiffness matrix may be obtained at the end of the iteration.

Dropping the subscripts in Eq. (39) and differentiating the equation yields

$$\dot{\boldsymbol{\sigma}} = \mathbf{D}_e \dot{\boldsymbol{\varepsilon}} - \dot{\lambda} \mathbf{D}_e \mathbf{b} - \Delta\lambda \mathbf{D}_e \frac{\partial \mathbf{b}}{\partial \boldsymbol{\sigma}} \dot{\boldsymbol{\sigma}} \quad (40)$$

Rearrangement and abbreviation of Eq. (40) yields

$$\dot{\boldsymbol{\sigma}} = \left(\mathbf{I} + \Delta\lambda \mathbf{D}_e \frac{\partial \mathbf{b}}{\partial \boldsymbol{\sigma}} \right)^{-1} \mathbf{D}_e (\dot{\boldsymbol{\varepsilon}} - \dot{\lambda} \mathbf{b}) = \mathbf{R} (\dot{\boldsymbol{\varepsilon}} - \dot{\lambda} \mathbf{b}) \quad (41)$$

where $\mathbf{R} = [\mathbf{I} + \Delta\lambda \mathbf{D}_e (\partial \mathbf{b} / \partial \boldsymbol{\sigma})]^{-1} \mathbf{D}_e$; and $(\partial \mathbf{b} / \partial \boldsymbol{\sigma}) = (\partial^2 Q / \partial \boldsymbol{\sigma}^2)$ is the second-order derivative of the potential function, with its specific form provided in detail in Appendix I.

To make the current stress σ lie on the yield surface, $\dot{F} = 0$ must be met. Namely, the consistent condition of the yield function requires

$$\dot{F} = \mathbf{a}^T \dot{\sigma} - A' \dot{\lambda} = 0 \quad (42)$$

where $\mathbf{a} = \partial F / \partial \sigma$ is the first-order derivative of the yield function (also known as the plastic flow vector), with its specific form provided in detail in Appendix I.

Substitution of Eq. (41) into Eq. (42) gives the following expression of $\dot{\lambda}$:

$$\dot{\lambda} = \frac{\mathbf{a}^T \mathbf{R} \dot{\epsilon}}{\mathbf{a}^T \mathbf{R} \mathbf{b} + A'} \quad (43)$$

Substitution of Eq. (43) into Eq. (41) yields

$$\dot{\sigma} = \left(\mathbf{R} - \frac{\mathbf{R} \mathbf{b} \mathbf{a}^T \mathbf{R}}{\mathbf{a}^T \mathbf{R} \mathbf{b} + A'} \right) \dot{\epsilon} = \mathbf{D}_{ct} \dot{\epsilon} \quad (44)$$

where \mathbf{D}_{ct} = consistent stiffness matrix. The rock or rock mass was regarded as an elastic-perfectly plastic material in this study, and therefore $A' = 0$.

Return Scheme in Tensile-Stress Zone

For consistency with the previous sections, the return scheme is conducted in any meridian plane (Fig. 8) with $I_1/\sqrt{3} - \sqrt{2J_2}$ rather than $p-q$ as the axes as in the literature (Wan 1992). Hoek (1983) pointed out that the uniaxial tensile strengths of fragile materials like rocks are equal to their biaxial tensile strengths, so if the experimental uniaxial or biaxial tensile strength of a rock is σ_t [usually less than the theoretical strength denoted as

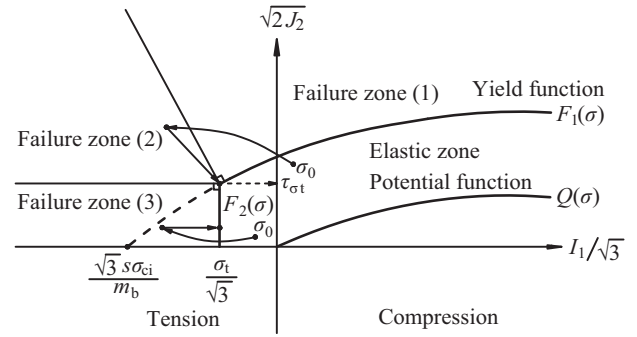


Fig. 8. Stress return modes.

Eq. (6)], then the yield function of tension cutoff can be defined as

$$F(\sigma) = \frac{I_1 - \sigma_t}{\sqrt{3}} = 0 \quad (45)$$

and it is plotted as the vertical line $F_2(\sigma)$ in Fig. 8. As a result, as shown in Fig. 8, $F_1(\sigma)$ [representing Eq. (34)] in conjunction with $F_2(\sigma)$ divides the whole failure region into three zones. Apparently, when a trial stress falls in Failure Zone 1, the previous return-mapping algorithm based on the general stress space will be used naturally. However, if the trial stress shoots far out in the tensile-stress zones including Failure Zones 2 and 3, then the return scheme proposed by Wan (1992) will be employed. In other words, if the trial stress falls in Failure Zone 2, it will be pulled back to the vertex that is the intersection of the Hoek-Brown yield surface or its transitional arc with the tension cutoff surface. Take the C1 continuous circular arc, for example; the vertex is given as

$$\begin{aligned} \left(\frac{I_1}{\sqrt{3}} \right)_t &= \frac{\sigma_t}{\sqrt{3}} \\ (\sqrt{2J_2})_t &= \frac{\sqrt{2m_b^2 \sigma_{ci}^2 \left(\cos \theta - \frac{\sin \theta}{\sqrt{3}} \right)^2 - 32 \cos^2 \theta \left(\frac{1}{3} \sigma_t m_b \sigma_{ci} - s \sigma_{ci}^2 \right) - \sqrt{2} m_b \sigma_{ci} \left(\cos \theta - \frac{\sin \theta}{\sqrt{3}} \right)}}{8 \cos^2 \theta} - \theta_t \geq \theta \leq \theta_t \end{aligned} \quad (46)$$

or

$$\begin{aligned} \left(\frac{I_1}{\sqrt{3}} \right)_t &= \frac{\sigma_t}{\sqrt{3}} \\ (\sqrt{2J_2})_t &= \sqrt{x_{oc}^2 + y_{oc}^2} \cos(30^\circ - \theta) + \sqrt{(x_{oc} - x_c)^2 + (y_{oc} - y_c)^2 - (x_{oc}^2 + y_{oc}^2) \sin^2(30^\circ - \theta)} = 0 \end{aligned} \quad \theta_t < \theta \leq 30^\circ \quad (47)$$

or

$$\begin{aligned} \left(\frac{I_1}{\sqrt{3}} \right)_t &= \frac{\sigma_t}{\sqrt{3}} \\ (\sqrt{2J_2})_t &= y_{ot} \cos(30^\circ + \theta) - \sqrt{x_t^2 + (y_{ot} - y_t)^2 - y_{ot}^2 \sin^2(30^\circ + \theta)} \end{aligned} \quad -30^\circ \leq \theta < -\theta_t \quad (48)$$

From Eqs. (46)–(48), it may be found that the location of a vertex is related to the Lode angle θ . Alternatively, if the trial stress

falls in Failure Zone 3, as shown in Fig. 8, it will be pulled back to $F_2(\sigma)$ in a direction parallel to the horizontal axis.

So far the stress adjustment schemes in the tensile-stress zones have been fulfilled in the meridian plane, but they were based on the principal stresses. The next problem is how to convert known principal stresses into stress vectors in the general stress space to facilitate numerical implementation. This can be achieved by constructing a conversion matrix. For isotropic problems, the coordinate system may not be considered in the calculations of the stress update and stiffness matrix because in the process of stress returns, shear stresses are always zero, and the direction of principal stresses do not change. Thus, the directional matrix may be determined by the predictor stress, and then it may be used to convert the updated stress into the general stress space. The stress components in the general stress space have the following relationship with the principal stresses:

$$d\{\boldsymbol{\sigma}\}_{6 \times 1} = [\mathbf{T}_{\sigma}]_{6 \times 3} d\{\boldsymbol{\sigma}_i\}_{3 \times 1} \quad (49)$$

where $\{\boldsymbol{\sigma}\}_{6 \times 1} = [\sigma_x, \sigma_y, \sigma_z, \tau_{xy}, \tau_{xz}, \tau_{yz}]^T$; $\{\boldsymbol{\sigma}_i\}_{3 \times 1} = [\sigma_1, \sigma_2, \sigma_3]^T$; and

$$[\mathbf{T}_{\sigma}]_{6 \times 3} = \begin{bmatrix} l_1^2 & l_2^2 & l_3^2 & l_1 l_2 & l_1 l_3 & l_2 l_3 \\ m_1^2 & m_2^2 & m_3^2 & m_1 m_2 & m_1 m_3 & m_2 m_3 \\ n_1^2 & n_2^2 & n_3^2 & n_1 n_2 & n_1 n_3 & n_2 n_3 \end{bmatrix}^T \quad (50)$$

where (l_1, l_2, l_3) , (m_1, m_2, m_3) , and (n_1, n_2, n_3) are the directional cosines of σ_1 , σ_2 , and σ_3 with respect to the x -, y -, and z -axes, respectively. Solving the eigenequation of the stress vector yields

$$l_1 = \frac{1}{D_1} [(\sigma_1 - \sigma_y)\tau_{xz} + \tau_{xy}\tau_{yz}] \quad (51)$$

$$l_2 = \frac{1}{D_1} [(\sigma_1 - \sigma_x)\tau_{yz} + \tau_{xy}\tau_{xz}] \quad (52)$$

$$l_3 = \frac{1}{D_1} [(\sigma_1 - \sigma_x)(\sigma_1 - \sigma_y) - \tau_{xy}^2] \quad (53)$$

$$\text{where } D_1 = \sqrt{[\tau_{xy}\tau_{yz} + (\sigma_1 - \sigma_y)\tau_{xz}]^2 + [\tau_{xz}\tau_{xy} + (\sigma_1 - \sigma_x)\tau_{yz}]^2 + [(\sigma_1 - \sigma_x)(\sigma_1 - \sigma_y) - \tau_{xy}^2]^2} \quad (54)$$

and (m_1, m_2, m_3) and (n_1, n_2, n_3) have the same forms as (l_1, l_2, l_3) and may be obtained by just replacing σ_1 in Eqs. (51)–(54) with σ_2 and σ_3 , respectively. Thus, the directional matrix is determined, and then it may be multiplied with a group of new principal stresses updated in the principal stress space to obtain the stress components in the general stress space.

Development of UMAT in Abaqus

For ease of use, at present, a UMAT of the linear-elasticity and perfect-plasticity constitutive model complying with the C1 continuity modified combined Hoek-Brown criterion was developed in *Abaqus*. The subroutine was coded in Fortran language. At the beginning of each incremental step, the stress-vector matrixes and state variables of elements from the previous step will be passed on to the UMAT, and at the end of this incremental step, the stresses and state variables related to the solution need to be updated. In the UMAT, the Jacobian matrix of the constitutive relationship is defined by the variable DDSDD (i.e., $\partial \Delta \boldsymbol{\sigma} / \partial \Delta \boldsymbol{\epsilon}$); the real stresses and elastic and plastic strains may be obtained through iterations, and thereby state variables such as hardening parameter, volumetric modulus, and shear modulus. A full algorithm described previously must, of course, be provided in the subroutine by users. Fig. 9 shows the flowchart of the subroutine calling and algorithm. Elastic trial stresses inherently are in the state of general stresses, and their counterparts of principal stresses may be obtained by calling the utility routine SPRINC (*S*, *PS*, *LSTR*, *NDI*, *NSHR*) provided by *Abaqus* or directly solved by the relevant formulae.

Computational Examples

To verify the validity and reliability of the self-developed UMAT, numerical simulation tests for the conventional triaxial compression and uniaxial tension were carried out and compared with the results obtained by the equivalent Mohr-Coulomb criterion. Then, the

mechanical behavior of the wall rock of a tunnel after excavation was numerically analyzed and compared with the analytical solution.

Numerical Simulation Tests of Triaxial Compression

A standard cylindrical rock specimen with a height of 100 mm and a diameter of 50 mm was built numerically (Fig. 10). The model was discretized into 572 elements with the element type of three-dimensional (3D) quadratic 20-node of reduced-integration (C3D20R). The experimental data (Table 1 and Fig. 11) of the Darley Dale sandrock was quoted from the literature (Mogi 2007), and the associated flow rule was employed herein. Comparisons show that the linear Mohr-Coulomb criterion overestimated the strength of the rock in lower- and higher-stress states and underrated it in the intermediate-stress state. In contrast, the Hoek-Brown criterion gave the desired results in all stress states. The results of the triaxial numerical tests under three confined pressures (i.e., $\sigma_3 = 0, 20$, and 50 MPa) are plotted in Fig. 12. In the elastic-stress state, the stress-strain curves of the Mohr-Coulomb model were found to overlap with those of the Hoek-Brown model precisely. There were, however, different yield stresses between these two models. Apparently, the numerical computation strengths (numbers in the boxes in Fig. 12) obtained by the Hoek-Brown model were less than those obtained by the Mohr-Coulomb model when $\sigma_3 = 0$ and 50 MPa, but the instance was reversed when $\sigma_3 = 20$ MPa. This fully complies with the theoretical law as depicted in Fig. 11, and the computation strengths obtained by the Hoek-Brown model were found to coincide with the theoretical values.

Numerical Simulation Tests of Uniaxial Tension

The previous model could still be used here. The simulated results with the assumption that the experimental uniaxial tensile strength of the rock was $\sigma_3 = \sigma_t = 5$ MPa and that 2-mm tension displacement was applied along the axial direction of the model are shown in Fig. 13. The exact tensile strength was given

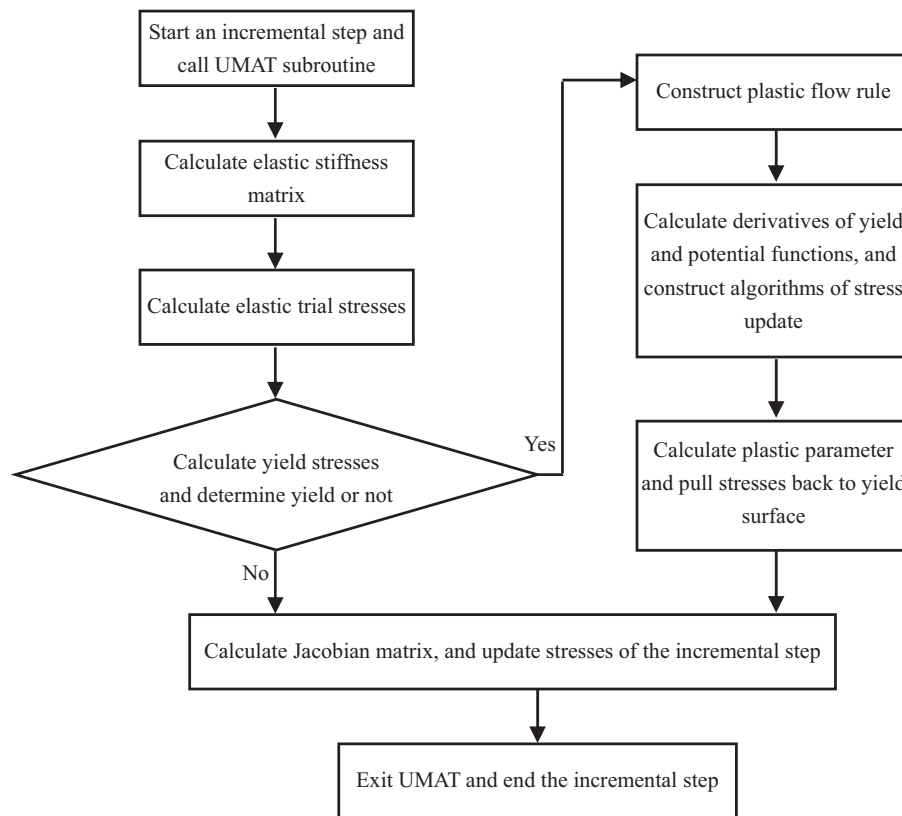


Fig. 9. Calling subroutine and flowchart of its algorithm.

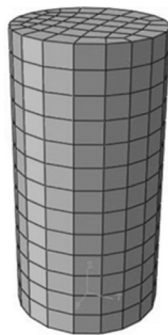


Fig. 10. Finite-element model of triaxial specimen and its meshes.

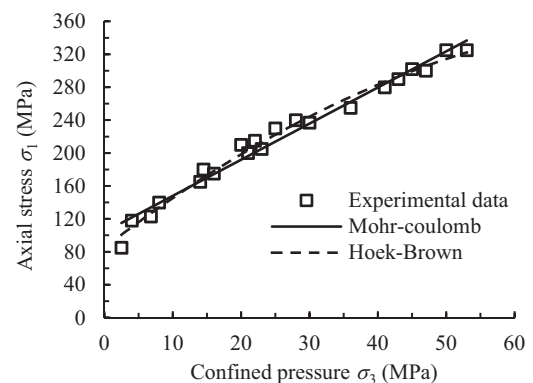


Fig. 11. Comparisons of theoretical fitting curves and triaxial test data.

Table 1. Mechanical parameters of Darley Dale sandrock

Parameter	Value
E (GPa)	4
ν	0.25
φ (°)	40.4
c (MPa)	21.5
m_b	15.9
s	1.0
a	0.5
σ_c (MPa)	80.0

by the modified combined Hoek-Brown criterion with tension cutoff, which was much lower than that of the classic Mohr-Coulomb criterion, and this is because the latter does not take tension cutoff into account.

Numerical Analysis of the Excavation of a Tunnel

A very common application of the Hoek-Brown criterion is to evaluate the wall-rock stability of tunnels after excavation, and it usually involves the evaluation of the potential failure zone and analysis of the stress distribution. For this reason, aiming at circular tunnels (Fig. 14), Carranza-Torres and Fairhurst (1999) presented a set of applicable theoretical formulas through a series of derivations, which have been verified to be able to truly reflect the mechanical responses of wall rock. In this part of the study, a circular tunnel was analyzed numerically, and the result was compared with the analytical solution.

In line with Carranza-Torres's (2004) study, for intact rock masses, the analytical solution to the previous question may be given by

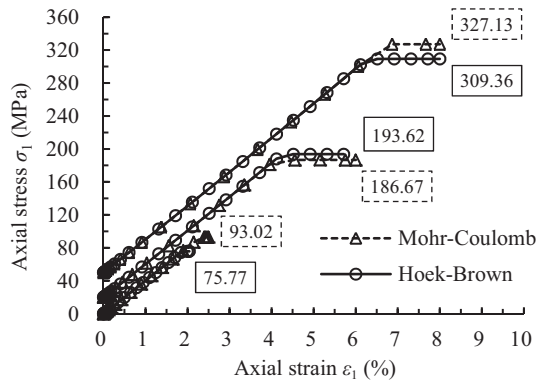


Fig. 12. Comparisons of simulated stress-strain curves.

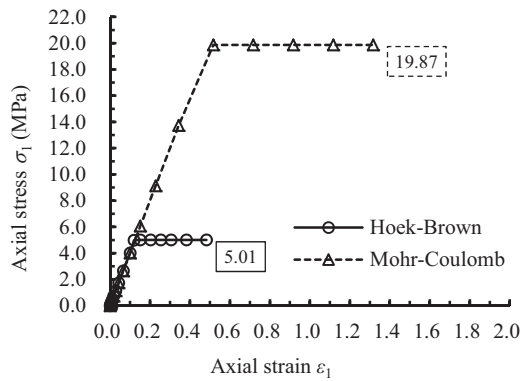


Fig. 13. Comparisons of stress-strain curves under uniaxial tension.

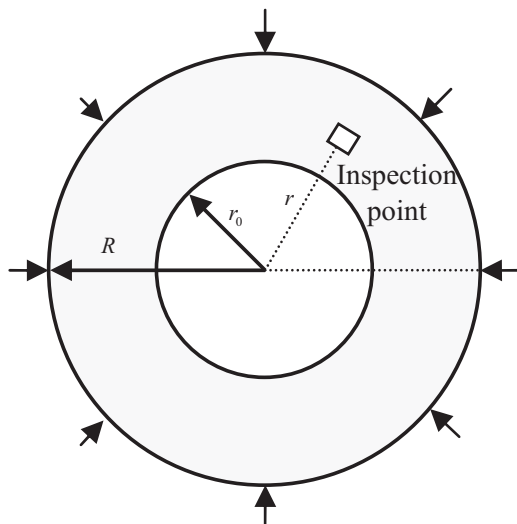


Fig. 14. Example of a tunnel excavation.

$$\begin{aligned}\sigma_r &= \left[S_r - \frac{s}{m_b^2} \right] m_b \sigma_{ci} \\ \sigma_\theta &= \left[S_\theta - \frac{s}{m_b^2} \right] m_b \sigma_{ci}\end{aligned}\quad (55)$$

where

$$S_r = \left[\sqrt{P_i^{cr}} + \frac{\ln(r/R_{pl})}{2} \right]^2 \quad (56)$$

$$S_\theta = S_r + \sqrt{S_r} \quad (57)$$

$$\frac{R_{pl}}{r_0} = \exp \left[2 \left(\sqrt{P_i^{ci}} - \sqrt{P_i} \right) \right] \quad (58)$$

$$P_i^{cr} = \left(\frac{1 - \sqrt{1 + 16S_0}}{4} \right)^2 \quad (59)$$

$$P_i = \frac{p_i}{m_b \sigma_{ci}} + \frac{s}{m_b^2} \quad (60)$$

$$S_0 = \frac{\sigma_0}{m_b \sigma_{ci}} + \frac{s}{m_b^2} \quad (61)$$

where σ_0 = far-field stress; p_i = internal pressure; S_0 , P_i = transformed stresses; R_{pl} = radius of the plastic zone; P_i^{cr} = critical internal pressure resulting in the advent of the plastic zone within the radius of R_{pl} ; r = radius of the inspection point; S_r = transformed radial stress; and S_θ = transformed hoop stress.

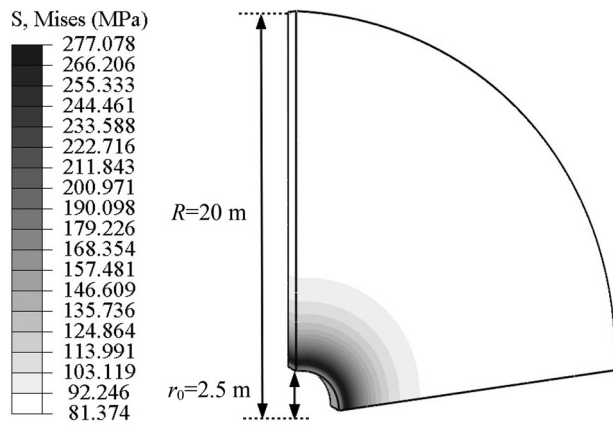
When using the above formulas to calculate the stress distribution, note that the location of an inspection point should meet the demand that $r \leq R_{pl}$; that is, the inspection point is within the plastic zone. For the elastic zone ($r > R_{pl}$), S_r , S_θ may be, respectively, solved by Eqs. (56) and (57):

$$S_r = S_0 - (S_0 - P_i^{cr}) \left(\frac{R_{pl}}{r} \right)^2 \quad (62)$$

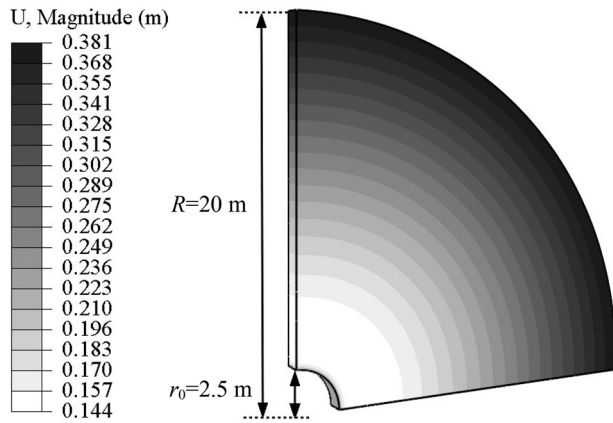
$$S_\theta = S_0 + (S_0 - P_i^{cr}) \left(\frac{R_{pl}}{r} \right)^2 \quad (63)$$

The mechanical properties of the rock in this example are as follows: $E = 5.7$ GPa, $\nu = 0.3$, $m_b = m_Q = 30$ MPa, $s = s_Q = 1.0$, $a = 0.5$, and $\sigma_{ci} = 100$ MPa. To ensure the advent of the palpable plastic zone, it is assumed that the confined pressure (radial pressure) around the outer border of the model $\sigma_0 = 200$ MPa and the inner pressure on the excavation border of the tunnel $p_i = 0$ MPa. The influence of the border effect needs to be considered in the selection of geometrical parameters; for this reason, the inner radius of the circular tunnel was assumed to be $r_0 = 2.5$ m. The influence of the border effect is not considered in the analytical solution presented by Carranza-Torres and Fairhurst (1999), and thus the model must be sufficiently large to eliminate this effect, and this can be seen from Eq. (56) as well. As per these assumed known conditions, on the outer border of the model, one may actually have $S_r = S_0 = 200$ MPa. From Eq. (56), the relative error between the analytical solution and the actual value may be obtained, which is roughly $(R_{pl}/r)^2$. Take $R = 20$ m as the outer radius of this model; then theoretically, $S_r = 195.8$ MPa, for which there is an error of 2.1% from the practical value.

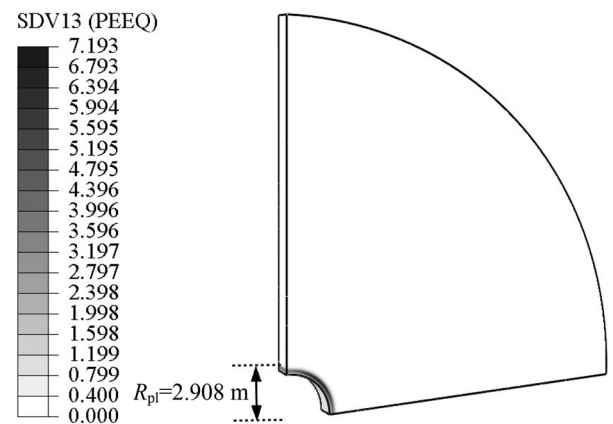
Given the symmetry of the model, applying the symmetrical border conditions, only a quarter of the model might be cut out to perform the computation. Some of the results are shown in Fig. 15. As shown in Fig. 15(c), the radius of the plastic zone R_{pl} obtained by the numerical computation was 2.908 m, whereas its analytical



(a)



(b)



(c)

Fig. 15. Posttreatment contours: (a) Mises stress; (b) radial displacement; and (c) equivalent plastic strain.

solution solved by Eq. (58) was 2.920 m, indicating that the relative error between these two was merely 0.4%. The analytical solutions of the radial and loop stresses of the inspection point can be readily solved by Eq. (55), and accordingly, the posttreatment results of the numerical solutions can be output by *Abaqus*. Fig. 16 provides comparisons of the analytical and numerical solutions. As is apparent, the numerical solutions were basically identical to the analytical ones, and the loop stress achieved its maximum at the interface between the elastic and plastic zones. Carranza-Torres and Fairhurst (1999) validated their analytical solutions in comparison with the numerical solutions obtained by *FLAC*. The comparisons in Fig. 16, however, show that the numerical implementation based

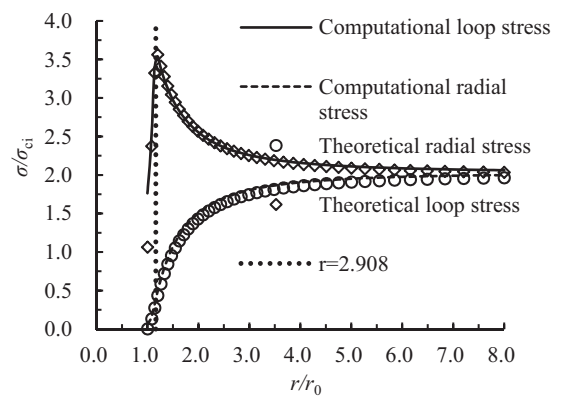


Fig. 16. Comparisons of radial and loop stresses.

on the modified combined Hoek-Brown criterion was successful and correct.

Conclusions

The C1 and C2 continuous smoothing approaches to the removal of the singularity at the apex of the Hoek-Brown yield and potential surfaces were presented, sequentially, and were shown to provide a sufficient physical approximation with clarity and simplicity and make the transition from one surface to another smooth and continuous. It has been rigorously proved that the numerical singularity of the original Hoek-Brown yield criterion can be ideally circumvented by adopting the C2 continuous composite yield function (surface) because any indeterminate terms can be eliminated, and the first- and second-order derivatives of this yield surface can be explicitly determined. Furthermore, both the C1 and C2 continuous smoothing yield surfaces ensure a totally convex yield surface. It is worth mentioning that the C2 continuous smoothing approach proposed in this article possesses universality, and as a result, it may also be applied in such a yield criterion that can be explicitly expressed in terms of the polar coordinates ($\sqrt{2}J_2$, θ), for instance, the linear or parabolic [as proposed by Singh et al. (2011)] Mohr-Coulomb yield criterion.

In addition, a tension cutoff surface that intersects with both the Hoek-Brown yield surface and the transitional circular cones was also employed so that the combined failure criterion is able to truly take the property of the lower tensile strength of rocks or rock masses into account. For the convenience of comprehension and programming, all yield functions were defined in terms of stress invariants.

A fully implicit backward Euler integral regression algorithm was employed, which needs to solve both the first-order derivatives of the yield and potential functions and the second-order derivative of the potential function to construct the consistent stiffness matrix to ensure the accuracy and efficiency of convergence.

The examples of the numerical simulations of the conventional triaxial compression and uniaxial tension tests demonstrate that either the approach of the removal of singularities on the edges of the initial Hoek-Brown criterion or the tension cutoff approach on the low-tensile-stress zone is successful and reliable.

The example of the numerical analysis of the tunnel excavation shows that the calculated results by the self-developed UMAT in *Abaqus* were identical to the analytical solutions.

Appendix I. Proof of Removal of Singularity

Employing the backward Euler integral regression algorithm to construct the consistent stiffness matrix involves the first-order derivatives of the yield and potential functions and the second-order derivative of the potential function. To simplify the representation, assuming $Q = F$, then only the first-order derivative of the yield function and the second-order derivative of the potential function need to be provided herein. As mentioned previously, the proposed C1 continuous smoothing approach is a special case of the C2 continuity approach. Therefore, the derivation process was only conducted for the C2 continuous yield function.

Singularity Detection for First-Order Derivative of Yield Surface

As is well known, the first-order derivative of the yield function is the flow vector \mathbf{a} , which can be given by

$$\mathbf{a} = \frac{\partial F}{\partial \boldsymbol{\sigma}} = \frac{\partial F}{\partial I_1} \frac{\partial I_1}{\partial \boldsymbol{\sigma}} + \frac{\partial F}{\partial \sqrt{J_2}} \frac{\partial \sqrt{J_2}}{\partial \boldsymbol{\sigma}} + \frac{\partial F}{\partial \theta} \frac{\partial \theta}{\partial J_3} \frac{\partial J_3}{\partial \boldsymbol{\sigma}} \\ = C_1 \mathbf{a}_1 + C_2 \mathbf{a}_2 + C_3 \mathbf{a}_3 \quad (64)$$

where

$$\mathbf{a}_1^T = \frac{\partial I_1}{\partial \boldsymbol{\sigma}} = \{1 \quad 1 \quad 1 \quad 0 \quad 0 \quad 0\}^T \\ \mathbf{a}_2^T = \frac{\partial \sqrt{J_2}}{\partial \boldsymbol{\sigma}} = \frac{1}{2\sqrt{J_2}} \{s_x \quad s_y \quad s_z \quad 2\tau_{xy} \quad 2\tau_{xz} \quad 2\tau_{yz}\}^T \\ \mathbf{a}_3^T = \frac{\partial J_3}{\partial \boldsymbol{\sigma}} = \begin{Bmatrix} s_y s_z - \tau_{yz}^2 \\ s_x s_z - \tau_{xz}^2 \\ s_x s_y - \tau_{xy}^2 \\ 2(\tau_{yz} \tau_{xz} - s_z \tau_{xy}) \\ 2(\tau_{xy} \tau_{yz} - s_y \tau_{xz}) \\ 2(\tau_{xz} \tau_{xy} - s_x \tau_{yz}) \end{Bmatrix} + \frac{J_2}{3} \begin{Bmatrix} 1 \\ 1 \\ 1 \\ 0 \\ 0 \\ 0 \end{Bmatrix}$$

and

$$C_1 = \frac{\partial F}{\partial I_1}, C_2 = \left(\frac{\partial F}{\partial \sqrt{J_2}} - \frac{\tan 3\theta}{\sqrt{J_2}} \frac{\partial F}{\partial \theta} \right), C_3 = \frac{-\sqrt{3}}{2 \cos 3\theta} \frac{1}{J_2^{3/2}} \frac{\partial F}{\partial \theta} \quad (65)$$

Determining the constants C_1 , C_2 , and C_3 involves the differentiation of the yield function with respect to the stress invariants and Lode angle. The purpose of this appendix is, however, to verify whether the numerical singularity can be overcome. Hence, the detailed derivations of these constants are not necessary and will not be given here. Through a plain differential processing of Eq. (34), it is shown that the numerical singular problem in the original yield function results from C_2 and C_3 in Eq. (65), as $\tan 3\theta$ and $1/\cos 3\theta$ tend to infinity at $\theta = \pm 30^\circ$; that is, C_2 and C_3 become indeterminate on the corners of the hexagonal surface. This problem can be resolved by replacing the original yield surface with the arc yield surface when the Lode angle gets close enough to $\pm 30^\circ$ (i.e., $\theta > \theta_t$ or $\theta < -\theta_t$). Consequently, the key issue is to verify whether the arc yield function can overcome the problem.

Because the second and third piecewise functions in Eq. (34) represent two arc segments, the following two cases need to be considered separately.

Case 1, for $\theta_t < \theta \leq 30^\circ$ [relative to Eq. (34)]:

$$C_2 = \sqrt{2} + b_1 \frac{\tan 3\theta}{\sqrt{J_2}} \\ \times \left[O' O_c \sin(30^\circ - \theta) + \frac{O' O_c^2 \sin(30^\circ - \theta) \cos(30^\circ - \theta)}{\sqrt{r_c^2 - O' O_c^2 \sin^2(30^\circ - \theta)}} \right] \\ + 6c_1 \frac{\sin^2 3\theta}{\sqrt{J_2}} \quad (66)$$

$$C_3 = \frac{\sqrt{3}b_1}{2J_2^{3/2} \cos 3\theta} \\ \times \left[O' O_c \sin(30^\circ - \theta) + \frac{O' O_c^2 \sin(30^\circ - \theta) \cos(30^\circ - \theta)}{\sqrt{r_c^2 - O' O_c^2 \sin^2(30^\circ - \theta)}} \right] \\ + \frac{3\sqrt{3}c_1}{J_2^{3/2}} \sin 3\theta \quad (67)$$

where $O' O_c$ and r_c are given by Eqs. (19) and (20), respectively. Note that when $\lim_{\theta \rightarrow 30^\circ} [\tan 3\theta \sin(30^\circ - \theta)] = 1/3$, C_2 approaches the extremum on the left side with $\theta \rightarrow 30^\circ$. Furthermore, when $\lim_{\theta \rightarrow 30^\circ} [\sin(30^\circ - \theta) / \cos 3\theta] = 1/3$, C_3 approaches the extremum on the left side with $\theta \rightarrow 30^\circ$:

$$C_2 \rightarrow \left(\sqrt{2} + b_1 \frac{O' O_c}{3\sqrt{J_2}} \left[1 + \frac{O' O_c}{r_c} \right] + \frac{6c_1}{\sqrt{J_2}} \right)_- \quad (68)$$

$$C_3 \rightarrow \left(b_1 \frac{\sqrt{3}O' O_c}{6J_2^{3/2}} \left[1 + \frac{O' O_c}{r_c} \right] + \frac{3\sqrt{3}c_1}{J_2^{3/2}} \right)_- \quad (69)$$

where no indeterminate terms occur. That means the constants C_2 and C_3 may now have definite values even if the Lode angle approaches or even equals 30° .

Case 2, for $-30^\circ \leq \theta < -\theta_t$ [relative to Eq. (34)]:

$$C_2 = \sqrt{2} - b_2 \frac{\tan 3\theta}{\sqrt{J_2}} \\ \times \left[O' O_t \sin(30^\circ + \theta) + \frac{O' O_t^2 \sin(30^\circ + \theta) \cos(30^\circ + \theta)}{\sqrt{r_t^2 - O' O_t^2 \sin^2(30^\circ + \theta)}} \right] \\ + 6c_2 \frac{\sin^2 3\theta}{\sqrt{J_2}} \quad (70)$$

$$C_3 = -\frac{\sqrt{3}b_2}{2J_2^{3/2} \cos 3\theta} \\ \times \left[O' O_t \sin(30^\circ + \theta) + \frac{O' O_t^2 \sin(30^\circ + \theta) \cos(30^\circ + \theta)}{\sqrt{r_t^2 - O' O_t^2 \sin^2(30^\circ + \theta)}} \right] \\ + \frac{3\sqrt{3}c_2}{J_2^{3/2}} \sin 3\theta \quad (71)$$

where $O'O_t$ and r_t are given by Eqs. (24) and (25), respectively. Note that $\lim_{\theta \rightarrow -30^\circ} [\tan 3\theta \sin(30^\circ + \theta)] = -1/3$. Thus, C_2 approaches the extremum on the right side with $\theta \rightarrow -30^\circ$. Conversely, given $\lim_{\theta \rightarrow -30^\circ} [\sin(30^\circ + \theta)/\cos 3\theta] = 1/3$, C_3 approaches the extremum on the right side with $\theta \rightarrow -30^\circ$:

$$C_2 \rightarrow \left(\sqrt{2} - b_2 \frac{O'O_t}{3\sqrt{J_2}} \left[1 + \frac{O'O_t}{r_t} \right] + \frac{6c_2}{\sqrt{J_2}} \right)_+ \quad (72)$$

$$C_3 \rightarrow \left(-b_2 \frac{\sqrt{3}O'O_t}{6J_2^{3/2}} \left[1 + \frac{O'O_t}{r_t} \right] + \frac{3\sqrt{3}c_2}{J_2^{3/2}} \right)_+ \quad (73)$$

Likewise, the constants C_2 and C_3 may always have definite values as well.

By now, one can find those singular terms in Eq. (65) can be eliminated by using the C2 continuous rounding yield surface or the C1 continuous scheme [i.e., let $b_1 = b_2 = 1$ and $a_1 = c_1 = a_2 = c_2 = 0$ in Eq. (34)].

Singularity Detection for Second-Order Derivative of Yield Surface

The second-order derivative of the plastic potential function is given by

$$\begin{aligned} \frac{\partial \mathbf{b}}{\partial \sigma} &= \frac{\partial^2 Q}{\partial \sigma^2} \\ &= \frac{\partial C_1}{\partial \sigma} \frac{\partial I_1}{\partial \sigma} + \frac{\partial C_2}{\partial \sigma} \frac{\partial \sqrt{J_2}}{\partial \sigma} + C_2 \frac{\partial^2 \sqrt{J_2}}{\partial \sigma^2} + \frac{\partial C_3}{\partial \sigma} \frac{\partial J_3}{\partial \sigma} + C_3 \frac{\partial^2 J_3}{\partial \sigma^2} \end{aligned} \quad (74)$$

where

$$\begin{aligned} \frac{\partial^2 J_3}{\partial \sigma^2} &= \frac{1}{3} \cdot \begin{bmatrix} s_x - s_y - s_z & & & & & \\ 2s_z & s_y - s_x - s_z & & & & \text{sym} \\ 2s_y & 2s_x & s_z - s_x - s_y & & & \\ 2\tau_{xy} & 2\tau_{xy} & -4\tau_{xy} & -6s_z & & \\ 2\tau_{xz} & -4\tau_{xz} & 2\tau_{xz} & 6\tau_{yz} & -6s_y & \\ -4\tau_{yz} & 2\tau_{yz} & 2\tau_{yz} & 6\tau_{xz} & 6\tau_{xy} & -6s_x \end{bmatrix} \\ \frac{\partial^2 \sqrt{J_2}}{\partial \sigma^2} &= \frac{1}{\sqrt{J_2}} \cdot \begin{bmatrix} \frac{1}{3} - \frac{s_x^2}{4J_2} & & & & & \\ -\frac{1}{6} - \frac{s_x s_y}{4J_2} & \frac{1}{3} - \frac{s_y^2}{4J_2} & & & & \text{sym} \\ -\frac{1}{6} - \frac{s_x s_z}{4J_2} & -\frac{1}{6} - \frac{s_y s_z}{4J_2} & \frac{1}{3} - \frac{s_z^2}{4J_2} & & & \\ -\frac{\tau_{xy} s_x}{2J_2} & -\frac{\tau_{xy} s_y}{2J_2} & -\frac{\tau_{xy} s_z}{2J_2} & 1 - \frac{\tau_{xy}^2}{J_2} & & \\ -\frac{\tau_{xz} s_x}{2J_2} & -\frac{\tau_{xz} s_y}{2J_2} & -\frac{\tau_{xz} s_z}{2J_2} & -\frac{\tau_{xz} \tau_{xy}}{2J_2} & 1 - \frac{\tau_{xz}^2}{J_2} & \\ -\frac{\tau_{yz} s_x}{2J_2} & -\frac{\tau_{yz} s_y}{2J_2} & -\frac{\tau_{yz} s_z}{J_2} & -\frac{\tau_{yz} \tau_{xy}}{J_2} & -\frac{\tau_{yz} \tau_{xz}}{J_2} & 1 - \frac{\tau_{yz}^2}{J_2} \end{bmatrix} \end{aligned}$$

and

$$\frac{\partial C_1}{\partial \sigma} = \frac{\partial C_1}{\partial I_1} \frac{\partial I_1}{\partial \sigma} + \frac{\partial C_1}{\partial \sqrt{J_2}} \frac{\partial \sqrt{J_2}}{\partial \sigma} + \frac{\partial C_1}{\partial \theta} \frac{\partial \theta}{\partial J_3} \frac{\partial J_3}{\partial \sigma} = C_{11} \frac{\partial I_1}{\partial \sigma} + C_{12} \frac{\partial \sqrt{J_2}}{\partial \sigma} + C_{13} \frac{\partial J_3}{\partial \sigma} \quad (75)$$

$$\frac{\partial C_2}{\partial \sigma} = \frac{\partial C_2}{\partial I_1} \frac{\partial I_1}{\partial \sigma} + \frac{\partial C_2}{\partial \sqrt{J_2}} \frac{\partial \sqrt{J_2}}{\partial \sigma} + \frac{\partial C_2}{\partial \theta} \frac{\partial \theta}{\partial J_3} \frac{\partial J_3}{\partial \sigma} = C_{21} \frac{\partial I_1}{\partial \sigma} + C_{22} \frac{\partial \sqrt{J_2}}{\partial \sigma} + C_{23} \frac{\partial J_3}{\partial \sigma} \quad (76)$$

$$\frac{\partial C_3}{\partial \sigma} = \frac{\partial C_3}{\partial I_1} \frac{\partial I_1}{\partial \sigma} + \frac{\partial C_3}{\partial \sqrt{J_2}} \frac{\partial \sqrt{J_2}}{\partial \sigma} + \frac{\partial C_3}{\partial \theta} \frac{\partial \theta}{\partial J_3} \frac{\partial J_3}{\partial \sigma} = C_{31} \frac{\partial I_1}{\partial \sigma} + C_{32} \frac{\partial \sqrt{J_2}}{\partial \sigma} + C_{33} \frac{\partial J_3}{\partial \sigma} \quad (77)$$

To save space, not all expressions for calculating the constants C_{ij} ($i, j = 1, 2, 3$) in Eqs. (75)–(77) will be given here. Through a plain algebraic calculation, it can be found that C_{11} , C_{21} , C_{31} , C_{12}

(because $C_{12} = C_{21}$), and C_{13} (because $C_{13} = C_{31}$) have a certain value, respectively. Thereby, only the concise expressions for C_{22} , C_{23} , C_{32} , and C_{33} are provided herein.

In addition, to determine those constants C_{ij} in Eqs. (75)–(77), likewise, two cases still need to be considered separately.

Case 1, for $\theta_t < \theta \leq 30^\circ$ [relative to Eq. (34)]:

$$C_{22} = -\frac{b_1}{J_2} [(B_1 + T_1)R_1 + B_1^2 R_2] - \frac{18c_1}{J_2} \sin^2 3\theta \quad (78)$$

$$C_{23} = \frac{-\sqrt{3}b_1}{2J_2^2} (T_2 R_1 + B_1 B_2 R_2) - \frac{6\sqrt{3}c_1}{J_2^2} \sin 3\theta \quad (79)$$

$$C_{32} = -\frac{\sqrt{3}b_1}{2J_2^2} [(3B_2 + T_3)R_1 + B_1 B_2 R_2] - \frac{18\sqrt{3}c_1}{J_2^2} \sin 3\theta \quad (80)$$

$$C_{33} = \frac{-3b_1}{4J_2^3} (T_4 R_1 + B_2^2 R_2) - \frac{27c_1}{2J_2^3} \cos 3\theta \quad (81)$$

where

$$\begin{cases} B_1 = \tan 3\theta \sin(30^\circ - \theta) \\ B_2 = \frac{\sin(30^\circ - \theta)}{\cos 3\theta} \end{cases} \quad (82)$$

$$\begin{cases} R_1 = O' O_c + \frac{O' O_c^2 \cos(30^\circ - \theta)}{\sqrt{r_c^2 - O' O_c^2 \sin^2(30^\circ - \theta)}} \\ R_2 = \frac{O' O_c^2}{\sqrt{r_c^2 - O' O_c^2 \sin^2(30^\circ - \theta)}} \left(1 - \frac{O' O_c^2 \cos^2(30^\circ - \theta)}{r_c^2 - O' O_c^2 \sin^2(30^\circ - \theta)} \right) \end{cases} \quad (83)$$

$$\begin{cases} T_1 = \frac{\partial B_1}{\partial \theta} \tan 3\theta, T_2 = \frac{\partial B_1}{\partial \theta} \frac{1}{\cos 3\theta} \\ T_3 = \frac{\partial B_2}{\partial \theta} \tan 3\theta, T_4 = \frac{\partial B_2}{\partial \theta} \frac{1}{\cos 3\theta} \end{cases} \quad (84)$$

In view of Appendix I, $B_1, B_2 \rightarrow 1/3$ when $\theta \rightarrow 30^\circ$. R_1 and R_2 are two constants that can be determined. Analogously, based on the limit analysis, the following results can be obtained:

$$\begin{cases} \lim_{\theta \rightarrow 30^\circ} T_1 = 19/27, \lim_{\theta \rightarrow 30^\circ} T_2 = 19/27 \\ \lim_{\theta \rightarrow 30^\circ} T_3 = -8/27, \lim_{\theta \rightarrow 30^\circ} T_4 = -8/27 \end{cases} \quad (85)$$

Thus, C_{22}, C_{23}, C_{32} , and C_{33} may now be calculated precisely without any indeterminate terms.

Case 2, for $-30^\circ \leq \theta < -\theta_t$ [relative to Eq. (34)]:

$$C_{22} = \frac{b_2}{J_2} [(B'_1 + T'_1)R'_1 + B'^2_1 R'_2] - \frac{18c_2}{J_2} \sin^2 3\theta \quad (86)$$

$$C_{23} = \frac{\sqrt{3}b_2}{2J_2^2} (T'_2 R'_1 + B'_1 B'_2 R'_2) - \frac{6\sqrt{3}c_2}{J_2^2} \sin 3\theta \quad (87)$$

$$C_{32} = \frac{\sqrt{3}b_2}{2J_2^2} [(3B'_2 + T'_3)R'_1 + B'_1 B'_2 R'_2] - \frac{18\sqrt{3}c_2}{J_2^2} \sin 3\theta \quad (88)$$

$$C_{33} = \frac{3b_2}{4J_2^3} (T'_4 R'_1 + B'^2_2 R'_2) - \frac{27c_2}{2J_2^3} \cos 3\theta \quad (89)$$

where

$$\begin{cases} B'_1 = \tan 3\theta \sin(30^\circ + \theta) \\ B'_2 = \frac{\sin(30^\circ + \theta)}{\cos 3\theta} \end{cases} \quad (90)$$

$$\begin{cases} R'_1 = O' O_t + \frac{O' O_t^2 \cos(30^\circ + \theta)}{\sqrt{r_t^2 - O' O_t^2 \sin^2(30^\circ + \theta)}} \\ R'_2 = \frac{O' O_t^2}{\sqrt{r_t^2 - O' O_t^2 \sin^2(30^\circ + \theta)}} \left(\frac{O' O_t^2 \cos^2(30^\circ + \theta)}{r_t^2 - O' O_t^2 \sin^2(30^\circ + \theta)} - 1 \right) \end{cases} \quad (91)$$

$$\begin{cases} T'_1 = \frac{\partial B'_1}{\partial \theta} \tan 3\theta, T'_2 = \frac{\partial B'_1}{\partial \theta} \frac{1}{\cos 3\theta} \\ T'_3 = \frac{\partial B'_2}{\partial \theta} \tan 3\theta, T'_4 = \frac{\partial B'_2}{\partial \theta} \frac{1}{\cos 3\theta} \end{cases} \quad (92)$$

Likewise, the following results can be obtained:

$$\begin{cases} \lim_{\theta \rightarrow 30^\circ} T_1 = -19/27, \lim_{\theta \rightarrow 30^\circ} T_3 = 19/27 \\ \lim_{\theta \rightarrow 30^\circ} T_5 = -8/27, \lim_{\theta \rightarrow 30^\circ} T_7 = 8/27 \end{cases} \quad (93)$$

Thus, C_{22}, C_{23}, C_{32} , and C_{33} can also be calculated precisely without indetermination problems. Overall, Eq. (34) depicts a C2 continuous composite yield function (surface) possessing both the explicit first- and second-order derivatives, so the numerical singular problem can be circumvented, and a global Newton-Raphson scheme will be implementable.

Here, it should be pointed out that to obtain the first- and second-order derivatives, some other terms, such as $\partial^2 K_c / \partial I_1^2$, $\partial^2 K_t / \partial I_1^2$, $\partial^2 x_{oc} / \partial I_1^2$, $\partial^2 y_{oc} / \partial I_1^2$, $\partial^2 y_{ot} / \partial I_1^2$, $\partial^3 \sqrt{2J_2} / \partial \theta \partial I_1^2$, $\partial^2 O' T_c / \partial I_1^2$, and $\partial^2 O' T_t / \partial I_1^2$, should be solved as well. To save space, they are not listed one by one in this article, but they can be readily deduced by mathematical computing tools (e.g., *MATLAB*) for interested readers.

Appendix II. Proof of Convexity

Looking at Fig. 2, the slope of a curve is given by Eq. (11), and the curve is convex by definition if $(d/d\theta)(dy/dx) \leq 0$ (van Eekelen 1980). After substitution of Eq. (11), the convexity condition for the curve $\sqrt{2J_2} = g(\theta)$ in the deviatoric plane can be given as

$$g^2(\theta) + 2g'^2(\theta) - g(\theta)g''(\theta) \geq 0 \quad (94)$$

The inequality can also be rewritten as $g(\theta)[g(\theta) - g''(\theta)] + 2g'^2(\theta) \geq 0$. Because $g(\theta) = \sqrt{2J_2}$ herein, $g(\theta)$ is always non-negative. Thus, the inequality always holds as long as $g''(\theta) \leq 0$. Next, the convexity examination is carried out in regard to the two piecewise smoothing yield surfaces because, essentially, the original Hoek-Brown yield surface is convex.

Proof of Convexity for C1 Continuous Rounding

At present, Eq. (27) can be written as

$$\sqrt{2J_2} = g(\theta) = \begin{cases} \frac{\sqrt{\frac{2}{3}[m_b\sigma_{ci}\cos(30^\circ + \theta)]^2 - 8\left(\frac{I_1}{3}m_b\sigma_{ci} - s\sigma_{ci}^2\right)\cos^2\theta - \frac{\sqrt{6}}{3}m_b\sigma_{ci}\cos(30^\circ + \theta)}}{4\cos^2\theta} & \text{for } -\theta_t \leq \theta \leq \theta_t \\ O'O_c \cos(30^\circ - \theta) + \sqrt{r_c^2 - (O'O_c \sin(30^\circ - \theta))^2} & \text{for } \theta_t < \theta \leq 30^\circ \\ O'O_t \cos(30^\circ + \theta) + \sqrt{r_t^2 - (O'O_t \sin(30^\circ + \theta))^2} & \text{for } -30^\circ \leq \theta < -\theta_t \end{cases} \quad (95)$$

The two piecewise functions expressed by Eq. (95) must satisfy the convexity condition for all $\theta \in [-30^\circ, -\theta_t]$ and $[\theta_t, 30^\circ]$, respectively.

Case 1, for $\theta \in [\theta_t, 30^\circ]$ [relative to Eq. (95)]:

$$g''(\theta) = -O'O_c \cos(30^\circ - \theta) - \frac{O'O_c^2 \cos(60^\circ - 2\theta)}{\sqrt{r_c^2 - O'O_c^2 \sin^2(30^\circ - \theta)}} - \frac{O'O_c^4 \cos^2(60^\circ - 2\theta)}{4[r_c^2 - O'O_c^2 \sin^2(30^\circ - \theta)]^{1.5}} \quad (96)$$

where $O'O_c$ is defined by Eq. (19) and is always greater than zero.

Thus, $g''(\theta) \leq 0$ always holds. That implies that the inequality in Eq. (94) always holds for $\theta \in [\theta_t, 30^\circ]$.

Case 2, for $\theta \in [-30^\circ, -\theta_t]$ [relative to Eq. (95)]:

$$g''(\theta) = -O'O_t \cos(30^\circ + \theta) - \frac{O'O_t^2 \cos(60^\circ + 2\theta)}{\sqrt{r_t^2 - O'O_t^2 \sin^2(30^\circ + \theta)}} - \frac{O'O_t^4 \cos^2(60^\circ + 2\theta)}{4[r_t^2 - O'O_t^2 \sin^2(30^\circ + \theta)]^{1.5}} \quad (97)$$

where $O'O_t$ is calculated by Eq. (24). If $O'O_t \geq 0$, $g''(\theta) \leq 0$, and the convexity condition is satisfied naturally. If $O'O_t \leq 0$, the problem needs to be dealt with further.

First, let $\kappa = -g(\theta)g''(\theta)$, and k can be explicitly expressed as

$$\begin{aligned} \kappa = [r_t^2 - O'O_t^2 \sin^2(30^\circ + \theta)] & \left[\frac{O'O_t \cos(30^\circ + \theta)}{\sqrt{r_t^2 - O'O_t^2 \sin^2(30^\circ + \theta)}} + \frac{O'O_t^2}{r_t^2 - O'O_t^2 \sin^2(30^\circ + \theta)} \right] \\ & + O'O_t^2 [\cos^2(30^\circ + \theta) - \sin^2(30^\circ + \theta)] \left[1 - \frac{O'O_t \cos(30^\circ + \theta)}{\sqrt{r_t^2 - O'O_t^2 \sin^2(30^\circ + \theta)}} \right] \\ & + \frac{O'O_t^4 \sin^2(30^\circ + \theta) \cos^2(30^\circ + \theta)}{r_t^2 - O'O_t^2 \sin^2(30^\circ + \theta)} \left[1 - \frac{O'O_t \cos(30^\circ + \theta)}{\sqrt{r_t^2 - O'O_t^2 \sin^2(30^\circ + \theta)}} \right] \end{aligned} \quad (98)$$

It is easy to find that the inequality in Eq. (94) always holds if k is nonnegative, particularly for all $\theta \in [-30^\circ, -\theta_t]$. To investigate this, and for the sake of brevity, an illustration is provided in Fig. 17. Meanwhile, given Eq. (98), the equivalent relationships $\sqrt{r_t^2 - O'O_t^2 \sin^2(30^\circ + \theta)} = AT_t$ and $|O'O_t| \cos(30^\circ + \theta) = AO'$ can be obtained readily. Herein, let $AO'/AT_t = t$, and then $t \in [0, 1]$. It is easy to find that $t = 0$ only when $r_t = r_t^1$ and $t \rightarrow 1$ when $AO' \gg O'T_t$ (e.g., when $r_t = r_t^1$). Thus, Eq. (95) can be rewritten as

$$\begin{aligned} \kappa = -l^2 \tan^2(30^\circ + \theta) t^5 + l^2 \tan^2(30^\circ + \theta) t^4 \\ - l^2 [1 - \tan^2(30^\circ + \theta)] t^3 + l^2 [2 - \tan^2(30^\circ + \theta)] t^2 - l^2 t \end{aligned} \quad (99)$$

where l denotes AT_t .

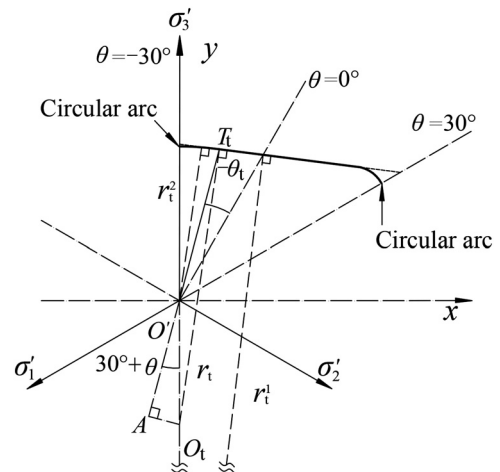


Fig. 17. Illustration of geometrical relations on interval $\theta \in [-\theta_t, -30^\circ]$ for C1 continuous approximation.

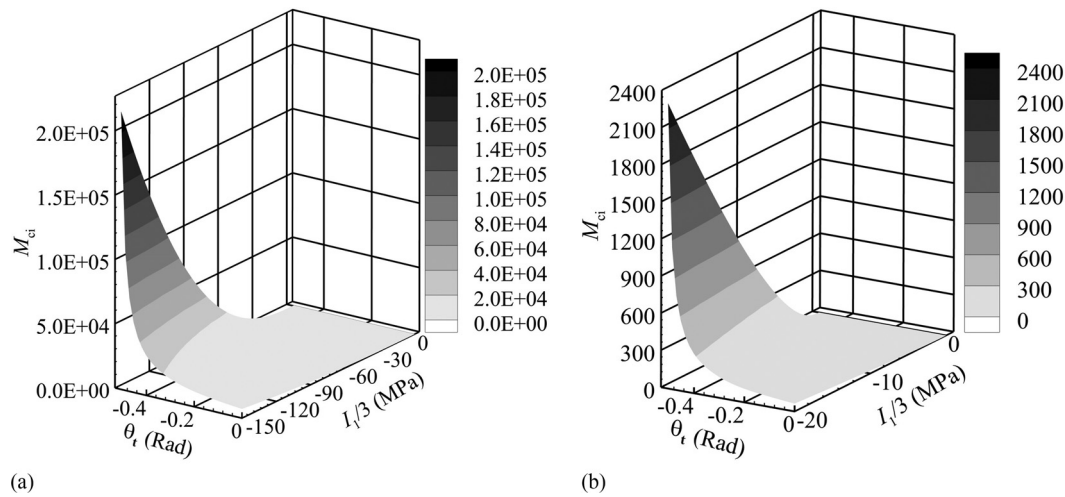


Fig. 18. Diagrams of minimum convexity indexes showing convexity on intervals $\theta \in [-30^\circ, -\theta_t]$ and θ_t ranging from 0 to -29° for C1 continuous rounding surfaces of two kinds of rock masses (unit of θ_t = radians): (a) Rock Mass A; and (b) Rock Mass B.

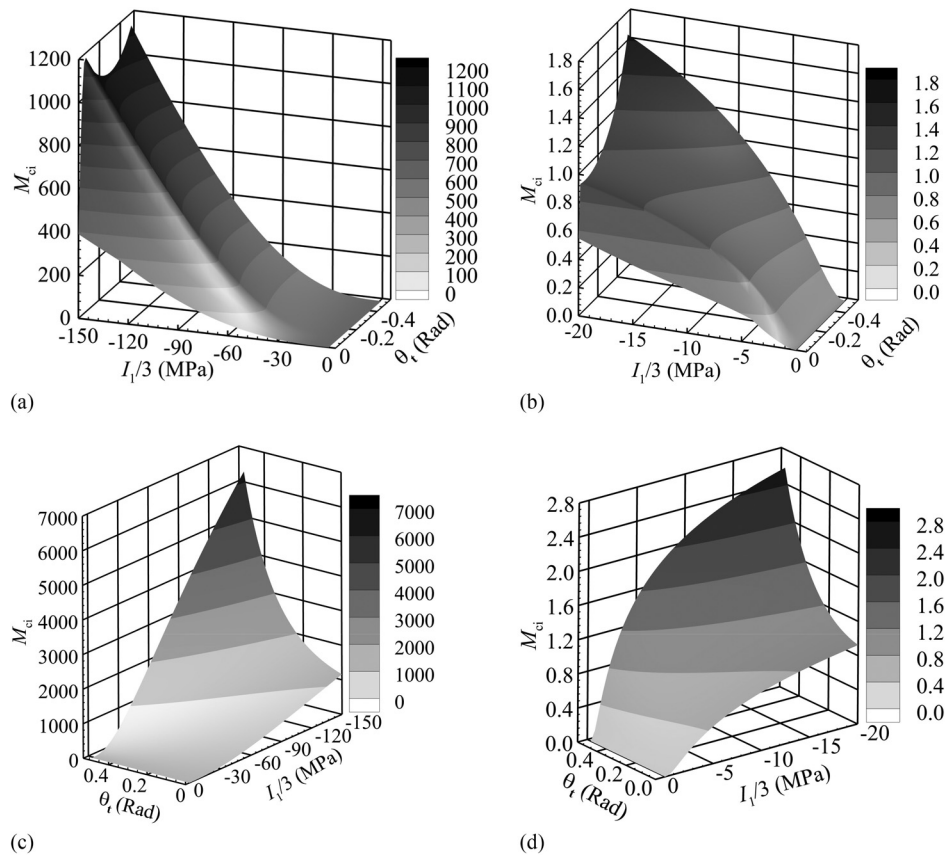


Fig. 19. Diagrams of minimum convexity indexes showing convexity on intervals $\theta \in [-30^\circ, -\theta_t]$ and $[\theta_t, 30^\circ]$ for C2 continuous smoothing surfaces of two kinds of rock masses (unit of θ_t = radians): (a) Rock Mass A and θ_t ranging from 0 to -29° ; (b) Rock Mass B and θ_t ranging from 0 to -29° ; (c) Rock Mass A and θ_t ranging from 0 to 29° ; and (d) Rock Mass B and θ_t ranging from 0 to 29° .

Through algebraic manipulation, it was found that the first-order derivative of κ is negative for all t on the interval $t \in [0, 1)$; one can conclude that κ approaches a minimum when t is unlimitedly close to 1, (i.e., $\kappa_{\min} \doteq \lim_{t \rightarrow 1} \kappa \doteq 0$). Accordingly, $\kappa = -g(\theta)g''(\theta) > 0$ always holds for $\theta \in [-30^\circ, -\theta_t]$, and as a result, the convexity condition is perpetually satisfied regardless of $O'O_c \geq 0$ or $O'O_c < 0$.

The authors think that the value on the left side of the inequality in Eq. (94) may be regarded as an index to examine the convexity of curves. Evidently, a curve must be convex if the minimum of the index is nonnegative. Therefore, in this study the minimum convexity index M_{ci} was introduced, which is defined as

$$M_{ci} = \min\{g^2(\theta) + 2g^2(\theta) - g(\theta)g''(\theta)\} \quad (100)$$

It is easy to infer that for a rock mass with known property parameters, the M_{ci} value of its smoothing yield surfaces is actually related to the transition angle θ_t and hydrostatic stresses $I_1/3$. Thus, the examination of convexity can be intuitively demonstrated by plotting the relationship between M_{ci} , θ_t , and $I_1/3$. Consider a high-quality rock mass (Rock Mass A) and a poor-quality rock mass (Rock Mass B), for example, with the property parameters $\sigma_{ci} = 150$ MPa, $m_i = 20$, $GSI = 75$ and $\sigma_{ci} = 20$ MPa, $m_i = 8$, $GSI = 30$ (Hoek and Brown 1997), respectively; the M_{ci} for their circular arc yield surfaces on the interval $\theta \in [-30^\circ, -\theta_t]$ was numerically computed with $I_1/3$ ranging from σ_{bt} [see Eq. (6)] to σ_{ci} . The results are plotted in Figs. 18(a) and (b), respectively. The results clearly show that M_{ci} was always nonnegative; that is, the circular arc yield surfaces for the two rock masses were convex in the whole region. Moreover, the results also show that M_{ci} increased with an increase in the absolute values of θ_t and/or $I_1/3$, and the increase rate became more and more remarkable.

Test of Convexity for C2 Continuous Smoothing

Likewise, Eq. (34) can be rewritten as

$$\sqrt{2J_2} = g(\theta) = \begin{cases} f_0(I_1/3, \theta) & \text{for } -\theta_t \leq \theta \leq \theta_t \\ a_1 + b_1 f_1(I_1/3, \theta, \theta_t) + c_1 \sin^2 3\theta & \text{for } \theta_t \leq \theta \leq 30^\circ \\ a_2 + b_2 f_2(I_1/3, \theta, \theta_t) + c_2 \sin^2 3\theta & \text{for } -30^\circ \leq \theta \leq -\theta_t \end{cases} \quad (101)$$

where a_1 , b_1 , c_1 and a_2 , b_2 , c_2 can be evaluated by Eqs. (31) and (33), respectively.

Unlike the previous section in which a rigorous algebraic operation and analysis was given first, the convexity for C2 continuous smoothing was tested only by numerical computation because deducing explicit expressions is a tedious process and will bring about some cumbersome formulations. Considering that the quality of rock masses is reflected by their property parameters (m_i , GSI , and σ_{ci}), by altering the values of these three parameters (e.g., m_i ranging from 5 to 35, GSI ranging from 25 to 100, and σ_{ci} ranging from 20 to 150 MPa, a large number of numerical computations were performed using *MATLAB*. It was found that M_{ci} was always nonnegative. Therefore, it can be concluded that a C2 continuous yield surface constructed according to the proposed method is convex for those rock masses whose property parameters are within the previously given ranges. For Rock Masses A and B mentioned previously, after smoothing their original Hoek-Brown yield surfaces by employing C2 continuous yield surfaces, similar numerical computations were carried out, and the visualized test results are shown in Fig. 19. The diagrams furnish some intuitional judgements: the arc yield surfaces to smooth the tensile corner where $-30^\circ \leq \theta \leq -\theta_t$ and the compressive corner where $\theta_t < \theta \leq 30^\circ$ maintained convexity for all values of θ_t for these two kinds of rock masses because M_{ci} was always nonnegative; M_{ci} showed a rapid growth with an increase of θ_t and $I_1/3$; and M_{ci} of Rock Mass A was much greater than that of Rock Mass B.

In sum, these numerical tests show that the convexity of the proposed C2 continuous arc yield surfaces can always be guaranteed no matter what the quality of a rock mass is.

Acknowledgments

The authors are grateful for the financial support of the Dept. of Transport of Fujian Province, China, for the research project (Grant 20130002).

Notation

The following symbols are used in this paper:

- \mathbf{A} = plastic flow vector related to yield function;
- A' = parameter reflecting hardening;
- a_n, a_{n+1} = plastic internal variables at time steps n and $n + 1$, respectively;
- $\mathbf{a}_1, \mathbf{a}_2, \mathbf{a}_3$ = components of \mathbf{a} ;
- $a_1, b_1, c_1, a_2, b_2, c_2$ = undetermined constant parameters used in C2 continuous approximation;
- \mathbf{B} = plastic flow vector related to potential function;
- c = cohesion;
- C_{ij} ($i, j = 1, 2, 3$) = constants in the expression of second-order derivative of potential function;
- C_1, C_2, C_3 = constants in the expression of plastic flow vector related to yield function;
- \mathbf{D}_{ct} = consistent stiffness matrix;
- \mathbf{D}_e = elasticity matrix;
- E = elastic modulus;
- F = yield function;
- I_1 = first stress invariant;
- J_2 = second deviatoric stress invariant;
- J_3 = third deviatoric stress invariant;
- M_{ci} = minimum convexity index;
- m_i, m_b, s, a = empirical parameters related to Hoek-Brown yield function;
- m_Q, s_Q = empirical parameters related to Hoek-Brown potential function;
- p = hydrostatic stress;
- Q = potential function;
- R_{pl} = radius of plastic zone;
- ν = Poisson's ratio;
- γ = unit weight;
- $\Delta \boldsymbol{\varepsilon}$ = increment of strain vector;
- $\Delta \lambda$ = plastic multiplier;
- $\Delta \boldsymbol{\sigma}$ = increment of stress vector;
- $\boldsymbol{\varepsilon}$ = stress vector;
- Θ = Lode angle of stress or strain;
- θ_t = transition Lode angle;
- $\boldsymbol{\sigma}$ = stress vector;
- σ_{bt} = biaxial or triaxial compressive strength of rock;
- σ_c = uniaxial compressive strength of rock;
- σ_{ci} = uniaxial compressive strength of the intact rock;
- $\boldsymbol{\sigma}_{n+1}^{\text{trial}}$ = trial elastic stress;
- σ_{ut} = uniaxial tensile strength of rock;
- $\dot{\sigma}, \dot{\varepsilon}, \dot{\lambda}, \dot{F}$ = variation rates of $\sigma, \varepsilon, \lambda, F$, respectively;
- $\tau_{\sigma c}$ = triaxial compressive strength;
- $\tau_{\sigma t}$ = triaxial tensile strength; and
- φ = angle of internal friction.

References

- Abbo, A. J., A. V. Lyamin, S. W. Sloan, and J. P. Hambleton. 2011. "A C2 continuous approximation to the Mohr-Coulomb yield surface." *Int. J. Solids Struct.* 48 (21): 3001–3010. <https://doi.org/10.1016/j.ijsolstr.2011.06.021>.
- Alejano, L. R., and A. Bobet. 2012. "Drucker-Prager criterion." *Rock Mech. Rock Eng.* 45 (6): 995–999. <https://doi.org/10.1007/s00603-012-0278-2>.
- Anyaeibunam, A. J. 2015. "Nonlinear power-type failure laws for geomaterials: Synthesis from triaxial data, properties, and applications." *Int. J. Geomech.* 15 (1): 0401436. [https://doi.org/10.1061/\(ASCE\)GM.1943-5622.0000348](https://doi.org/10.1061/(ASCE)GM.1943-5622.0000348).
- Baker, R. 2004. "Nonlinear Mohr envelopes based on triaxial data." *J. Geotech. Geoenviron. Eng.* 130 (5): 498–506. [https://doi.org/10.1061/\(ASCE\)1090-0241\(2004\)130:5\(498\)](https://doi.org/10.1061/(ASCE)1090-0241(2004)130:5(498)).
- Belytschko, T., W. K. Liu, and B. Moran. 2000. *Nonlinear finite elements for continua and structures*. Chichester, UK: Wiley.
- Benz, T., R. Schwab, R. A. Kauther, and P. A. Vermeer. 2008. "A Hoek-Brown criterion with intrinsic material strength factorization." *Int. J. Rock Mech. Min. Sci.* 45 (2): 210–222. <https://doi.org/10.1016/j.ijrmms.2007.05.003>.
- Borst, R. D., M. A. Crisfield, J. J. C. Remmers, and C. V. Verhoosel. 2012. *Non-linear finite element analysis of solid and structures*. 2nd ed. Chichester, UK: Wiley.
- Carranza-Torres, C. 2004. "Elasto-plastic solution of tunnel problems using the generalized form of the Hoek-Brown failure criterion." *Int. J. Rock Mech. Min. Sci.* 41 (1): 629–639. <https://doi.org/10.1016/j.ijrmms.2004.03.111>.
- Carranza-Torres, C., and C. Fairhurst. 1999. "The elasto-plastic response of underground excavations in rock masses that satisfy the Hoek-Brown failure criterion." *Int. J. Rock Mech. Min. Sci.* 36 (6): 777–809. [https://doi.org/10.1016/S0148-9062\(99\)00047-9](https://doi.org/10.1016/S0148-9062(99)00047-9).
- Charles, J. A., and M. M. Soares. 1984. "The stability of slopes with nonlinear failure envelopes." *Can. Geotech. J.* 21 (3): 397–406. <https://doi.org/10.1139/t84-044>.
- Clausen, J., and L. Damkilde. 2008. "An exact implementation of the Hoek-Brown criterion for elasto-plastic finite element calculations." *Int. J. Rock Mech. Min. Sci.* 45 (6): 831–847. <https://doi.org/10.1016/j.ijrmms.2007.10.004>.
- Clausen, J., L. Damkilde, and L. Andersen. 2006. "Efficient return algorithms for associated plasticity with multiple yield planes." *Int. J. Numer. Methods Eng.* 66 (6): 1036–1059. <https://doi.org/10.1002/nme.1595>.
- Dawson, E., K. H. You, and Y. J. Park. 2000. "Strength-reduction stability analysis of rock slopes using the Hoek-Brown failure criterion." In *Proc., Geo-Denver 2000*, 65–77. Reston, VA: ASCE.
- Drucker, D. C., and W. Prager. 1952. "Soil mechanics and plastic analysis or limit design." *Q. Appl. Math.* 10 (2): 157–165. <https://doi.org/10.1090/qam/48291>.
- Fu, W., and Y. Liao. 2010. "Non-linear shear strength reduction technique in slope stability calculation." *Comput. Geotech.* 37 (3): 288–298. <https://doi.org/10.1016/j.compgeo.2009.11.002>.
- Hoek, E. 1983. "Strength of jointed rock masses." *Géotechnique* 33 (3): 187–223. <https://doi.org/10.1680/geot.1983.33.3.187>.
- Hoek, E. 1994. "Strength of rock and rock masses." *ISRM News J.* 2 (2): 4–16.
- Hoek, E., and E. T. Brown. 1980. "Empirical strength criterion for rock masses." *J. Geotech. Eng. Div.* 106 (9): 1013–1035.
- Hoek, E., and E. T. Brown. 1997. "Practical estimates of rock mass strength." *Int. J. Rock Mech. Min. Sci.* 34 (8): 1165–1186. [https://doi.org/10.1016/S1365-1609\(97\)80069-X](https://doi.org/10.1016/S1365-1609(97)80069-X).
- Hoek, E., C. Carranza-Torres, and B. Corkum. 2002. "Hoek-Brown failure criterion—2002 edition." In *Proc., NARMS-TAC Conf.*, 267–273. Toronto: North American Rock Mechanics.
- Koiter, W. T. 1953. "Stress-strain relations uniqueness and variational theorems for elastic-plastic materials with a singular yield surface." *Q. Appl. Math.* 11 (3): 350–354. <https://doi.org/10.1090/qam/59769>.
- Lade, P. V., and J. M. Duncan. 1975. "Elastoplastic stress-strain theory for cohesionless soil." *J. Geotech. Eng. Div.* 101 (10): 1037–1053.
- Lefebvre, G. 1981. "Fourth Canadian geotechnical colloquium: Strength and slope stability in Canadian soft clay deposits." *Can. Geotech. J.* 18 (3): 420–442. <https://doi.org/10.1139/t81-047>.
- Matsuoka, H., and T. Nakai. 1974. "Stress-deformation and strength characteristics of soil under three different principal stresses." *Proc. Jpn. Soc. Civ. Eng.* 1974 (232), 59–70. https://doi.org/10.2208/jscej1969.1974.232_59.
- Menetrey, P. H., and K. J. Willam. 1995. "Triaxial failure criterion for concrete and its generalization." *Struct. J.* 92 (3): 311–318. <https://doi.org/10.14359/1132>.
- Mogi, K. 2007. *Experimental rock mechanics*. Abingdon, UK: Taylor & Francis.
- Nayak, G. C., and O. C. Zienkiewicz. 1972. "Convenient form of stress invariants for plasticity." *J. Struct. Div.* 98 (4): 949–953.
- Owen, D. R. J., and E. Hinton. 1980. *Finite elements in plasticity: Theory and practice*. Swansea, Wales: Pineridge.
- Ramamurthy, T., G. V. Rao, and K. S. Rao. 1988. "A non-linear strength criterion for rocks." In *Proc., 5th Australia-New Zealand Conf. on Geomechanics: Prediction versus Performance*, 247–252. Kolkata, India: Institution of Engineers.
- Ristinmaa, M., and J. Tryding. 1993. "Exact integration of constitutive equations in elasto-plasticity." *Int. J. Numer. Methods Eng.* 36 (15): 2525–2544. <https://doi.org/10.1002/nme.1620361503>.
- Simo, J. C., and R. L. Taylor. 1985. "Consistent tangent operators for rate-independent elastoplasticity." *Comput. Methods Appl. Mech. Eng.* 48 (1): 101–118. [https://doi.org/10.1016/0045-7825\(85\)90070-2](https://doi.org/10.1016/0045-7825(85)90070-2).
- Singh, M., A. Raj, and B. Singh. 2011. "Modified Mohr-Coulomb criterion for non-linear triaxial and polyaxial strength of intact rocks." *Int. J. Rock Mech. Min. Sci.* 48 (4): 546–555. <https://doi.org/10.1016/j.ijrmms.2011.02.004>.
- Thorsen, K. 2013. "Analytical failure prediction of inclined boreholes." *Int. J. Geomech.* 13 (3): 318–325. [https://doi.org/10.1061/\(ASCE\)GM.1943-5622.0000208](https://doi.org/10.1061/(ASCE)GM.1943-5622.0000208).
- Trivedi, A. 2013. "Estimating in situ deformation of rock masses using a hardening parameter and RQD." *Int. J. Geomech.* 13 (4): 348–364. [https://doi.org/10.1061/\(ASCE\)GM.1943-5622.0000215](https://doi.org/10.1061/(ASCE)GM.1943-5622.0000215).
- Van Eekelen, H. A. M. 1980. "Isotropic yield surfaces in three dimensions for use in soil mechanics." *Int. J. Numer. Anal. Methods Geomech.* 4 (1): 89–101. <https://doi.org/10.1002/nag.1610040107>.
- Wan, R. G. 1992. "Implicit integration algorithm for Hoek-Brown elastic-plastic model." *Comput. Geotech.* 14 (3): 149–177. [https://doi.org/10.1016/0266-352X\(92\)90031-N](https://doi.org/10.1016/0266-352X(92)90031-N).
- Yi, X., P. P. Valkó, and J. E. Russell. 2005. "Effect of rock strength criterion on the predicted onset of sand production." *Int. J. Geomech.* 5 (1): 66–73. [https://doi.org/10.1061/\(ASCE\)1532-3641\(2005\)5:1\(66\)](https://doi.org/10.1061/(ASCE)1532-3641(2005)5:1(66)).
- Zou, J. F., and S. Yu. 2016. "Theoretical solutions of a circular tunnel with the influence of the out-of-plane stress based on the generalized Hoek-Brown failure criterion." *Int. J. Geomech.* 16 (3): 06015006. [https://doi.org/10.1061/\(ASCE\)GM.1943-5622.0000547](https://doi.org/10.1061/(ASCE)GM.1943-5622.0000547).